國立臺灣大學理學院物理學研究所

碩士論文

Department of Physics

College of Science

National Taiwan University

Master Thesis

共振偶極-偶極交互作用於束縛原子的暗態邊帶冷卻中之影響

Role of Resonant Dipole-Dipole Interactions in Dark-State Sideband Cooling of Trapped Atoms

王重賢

Chung-Hsien Wang

指導教授: 林俊達 博士
任祥華 博士

Advisor: Guin-Dar Lin Ph.D.
Hsiang-Hua Jen Ph.D.

中華民國 112 年 7 月

July, 2023

doi:10.6342/NTU202300902

致謝

本論文是在任祥華博士和林俊達副教授共同指導下完成的，兩人在我研究過程及口試中都提供了不少想法及研究方向。也感謝任祥華實驗室的同事們，在論文寫作過程中爲我提供不少建議。最後也得感謝朋友和家人們的支持，給予我讀書研究的資本以及支持鼓勵。

doi:10.6342/NTU202300902

doi:10.6342/NTU202300902

摘要

長程的偶極-偶極相互作用在各種量子光學系統中起著至關重要的作用，尤其在量子模擬和計算方面具有重要意義。本論文重點探究共振偶極-偶極相互作用在暗態邊帶冷卻中的影響。我們首先分析了自由空間原子之間的共振偶極-偶極相互作用。然後，我們將分辨邊帶冷卻技術擴展到暗態冷卻方案，並通過利用光子介導的偶極-偶極相互作用在束縛原子中實現增強冷卻效果。通過將原子放置在特定的粒子間距上，我們實現了目標原子超越單個原子所能達到的優越冷卻性能。我們進一步探索了具有激光失諧和不同偶極極化角度的多原子設置，並識別出多個奇特間距，預測隨著原子數量的增加，冷卻性能將有適度的提高。我們的研究揭示了利用光子介導的遠程偶極-偶極相互作用冷卻原子的原理，爲克服可擴展量子計算和量子模擬中的冷卻限制提供機會。

關鍵字：偶極-偶極相互作用、束縛原子、暗態邊帶冷卻

doi:10.6342/NTU202300902

Abstract

Long-range dipole-dipole interactions, mediated by photons, play a crucial role in various quantum optics systems and are particularly relevant for quantum simulation and computation. This thesis focuses on exploring the impact of resonant dipole-dipole interactions in the context of dark-state sideband cooling. We begin by analyzing the resonant dipole-dipole interaction between free-space atoms. We then extend the resolved sideband cooling technique to the dark-state cooling scheme and demonstrate enhanced cooling in trapped atoms by leveraging photon-mediated dipole-dipole interactions. Through placing atoms at specific interparticle distances, we achieve superior cooling performance in the target atom beyond what is achievable by a single atom. We further explore multiatom setups with laser detuning and different light polarization angles and identify multiple magic spacings where moderate improvements in cooling performance are predicted with increasing numbers of atoms. Our research sheds light on the cooling of atoms utilizing light-induced long-range dipole-dipole interactions and provides opportunities for overcoming cooling limitations in scalable quantum computation and quantum simulations.

Keywords: dipole-dipole interactions, trapped atoms, dark-state sideband cooling

Contents

Page

致謝 i

摘要 iii

Abstract v

Contents vii

List of Figures ix

Chapter 1 Introduction 1

Chapter 2 Light-atom interaction 5

2.1 System of two level atoms and electric fields 6

2.2 Markov approximation for Open Quantum System 7

2.3 Photon-mediated dipole-dipole interaction 10

Chapter 3 Resolved sideband cooling 13

3.1 Atomic motion and sideband 14

3.2 Lamb-Dicke regime 16

3.3 Dark-state sideband cooling 18

3.4 Simulating method 22

Chapter 4 Enhancing sideband cooling via dipole-dipole interaction 25

4.1 Few atoms cases 26

4.2 Dipole polarization and magic spacings 30
4.3 Effect of laser detuning and collective frequency shift 32
4.4 Multiatom configurations 34
Chapter 5 Conclusion **37**
References **39**
Appendix A — Derivation of Photon - mediated Dipole-Dipole Interaction **49**

doi:10.6342/NTU202300902

List of Figures

2.1 Collective energy shift $g_{\mu\nu}$ (a) and decay rate $\gamma_{\mu\nu}$ (b) under various polarization angles $\cos\theta$ and atomic spacings ξ. The collective decay rate $\gamma_{\mu\nu}$ approaches single atom decay rate Γ while energy shift $g_{\mu\nu}$ diverges in short distance limit $\xi \to 0$. 12

4.1 A diagram illustrating the multi-atom enhanced sideband cooling mechanism utilizing RDDIs within an equilateral triangle configuration with an interparticle spacing denoted as s_{12}. A laser (indicated by the red beam and arrow) is directed at the target atom. This laser drives the red-sideband transition from state $|g,n\rangle$ to $|e,n-1\rangle$, cooling the atom towards state $|g,n-1\rangle$ through the process of spontaneous emission(indicated by green arrow). The spin-exchange interactions in RDDIs (blue arrow) flip the spins of other atoms via multiple light scatterings while conserving atomic excitation numbers. The remaining spectator atoms can act as coolants, which extracts excess heat from the target atom through RDDIs, providing a special cooling mechanism. The figure has been adapted from [1]. Permission to adapt granted by the authors. 27

doi:10.6342/NTU202300902

4.2 Enhanced sideband cooling and the determination of magic spacing for two- and three- atom's configurations. (a) depicts the collective frequency shift g_{12} and decay rate γ_{12} with polarization angle being perpendicular $\cos\theta = 0$, as a function of the atomic separation s_{12}, for several values within the range of λ. A vanishing g_{12} indicates the presence a magic spacing $s_m \approx 0.7133\lambda$. (b) shows the ratio of the phonon number of the target atom, $\langle n_1 \rangle_{multi}$ to the single atom's limit, $\langle n_1 \rangle_{single}$, in a multi-atom configuration, for atoms arranged in a line (indicated by blue-solid line) and an equilateral triangle shape (indicated by red-dashed line), as a function of s_{12} within λ. The sideband cooling parameters are set such that $\Delta = -\nu$, $\Gamma = 0.1\nu$, and $\eta\Omega_1 = 0.04\nu$. A maximal enhancement of cooling performance occurs at $s_{12} = s_m$. The figure has been adapted from [1] 28

4.3 Identification of magic spacings, along with the corresponding collective decay rate, and cooling enhancement in a two-atom case. (a) The plot shows solid lines denoting the (s_{12}, θ) values for which the frequency shifts $g_{12}(s_{12}, \theta)$ vanish, where θ is defined as the angle between the interatomic distance and the dipole moment direction. The identified magic spacings, labeled as A to F, showcase varied cooling behaviors under different parameters. (b) and (c) respectively show the corresponding collective decay rates γ_{12} and cooling enhancement. An inset plot in (c) clearly defines θ. Several magic spacings emerge at $g_{12} = 0$ while varying θ. The remaining system parameters remain the same as depicted in Figure 4.2. This figure has been adapted from [1] 31

doi:10.6342/NTU202300902

4.4 The demonstration showing how the efficiency of cooling is influenced by the detuning of the laser and the collective frequency shift. (a) A schematic diagram illustrates how the presence of non-zero collective frequency shift Ω_s affects the spin-exchange interactions (blue arrow), resulting in reduced cooling performance once the laser is set to the regular red-sideband condition (red arrow). (b) Cooling efficiency is depicted as a function of laser detuning and particle spacings for a two-atom system. (c) We consider an isosceles triangle configuration with equilateral interatomic distances being magic spacing $s_m \approx 0.71\lambda$, where the optimal enhancement is achieved at $\phi = \pi/3$ for the target atom at the apex, with negligible collective frequency shifts for all atoms. Other three-atom configurations at different angles ϕ, such as a line shape at $\phi = \pi$, exhibit a reduced exchange process due to non-vanishing Ω_s, resulting in reduced but still better cooling performance compared to the single-atom case. The remaining parameters are consistent with those described in Fig. 4.2. This figure has been adapted from [1] 33

4.5 Various 4- and 5-atom configurations, positioned at the center and vertices of a hexagon, are examined to investigate the effect on cooling enhancement. The target atom is located at the center of the hexagon, with the and the lattice spacing of this hexagon is set to be magic spacing s_m. The ratio of the normalized phonon occupation of the target atom in the multi-atom configuration, $\langle n_1\rangle_{multi}$, to the single-atom case, $\langle n_1\rangle_{single}$,which indicates the cooling performance, is measured. The obtained ratios, $0.863, 0.864, 0.842, 0.849$ and 0.890, for configurations (a-e) respectively, indicate a moderate enhancement in cooling compared to the cases of $N = 2$ and 3 shown in Figs. 4.2(b) and 4.4(c). This figure has been adapted from [1] 35

doi:10.6342/NTU202300902

國立臺灣大學

Chapter1

Introduction

In recent decades, advances in technology have enabled greater control over atom arrays, allowing for the development of increasingly sophisticated techniques for confining particles [2–5] and manipulating their interactions [6, 7]. While laser cooling is one of the most important of these techniques [8], which is used to reduce the micromotion of trapped atoms and ions beyond the limits of Doppler cooling, bringing them closer to their motional ground state. Such techniques have been experimentally demonstrated and are essential for a wide range of applications in fields such as quantum simulation [9–14] and quantum computation [15–20]. This is achieved by resolved sideband cooling [21–25]. By balancing the speed of an atom's red-sideband transition with its spontaneous emission, pepole are able to achieve cooling in the microkelvin range. This technique has been extended to multi-level systems using electromagnetic induced transparency (EIT) [26–32], which is referred to as dark-state sideband cooling.

In multi-atomic systems, cooling mechanisms become more complex due to the emergence of spin-phonon correlations through light-matter interactions. By treating photon modes as reservoir, the remaining atoms form an open quantum system. Following by

Markov approximation, the dynamics of this system can be described by a Lindblad master equation, consisting dissipation and collective spin-exchange process [20, 33–36]. These photon-mediated dipole-dipole interactions (DDIs) can be customized into a strong coupling regime using an atom-waveguide interface with the modification on photon modes in reservoir and thus the DDIs. The DDIs mediated by photons have been investigated in various systems, including guided modes [37], cavity-mediated atoms [38] and two atoms in an atom-waveguide interface [39]. DDI strongly influences the radiation properties of ensembles of atoms, causing modifications to the decay rate and collective Lamb shift on resonance lines [40–44]. These effects give rise to collective phenomena such as dipole-dipole forces [45] and superradiance [46–48], which have been used to develop a quantum heat engine that surpasses the Carnot limit [49]. It is the intrinsic loss properties that provides a valuable subject for the study of non-Hermitian physics, such as exceptional points in atomic samples [50]. Programming DDI is also being investigated for its applications in quantum simulations on complex coupling graphs [7].

In this study, we examine the contribution of dipole-dipole interactions to cooling of atomic ensembles, specifically in the context of sideband cooling in a finite-sized sample [1], which is possible to be realized by current trapping techniques like optical tweezer [51, 52]. The cooling scheme involves a two-level structure of atoms, which can also be constructed using three-level Λ-type atom coupled by two laser fields. We investigate how cooling performance changes when other atoms are nearby exchanging photons with the cooling target. By placing extra atoms at a interparticle distances during sideband cooling, we demonstrate that rescattering events in DDIs allows target atom to have superior cooling performance under the assumption of asymmetric driving conditions. We investigate cooling behaviors with different dipole polarization angles and laser detunings. We also

doi:10.6342/NTU202300902

find more magic spacings that enhance cooling and improve multiatom effects for specific configurations.

The rest of this thesis is organized as follows. We first introduce light-atom interaction in chapter 2, using Markov approximation on master equation in open quantum system to derive Linbladian dipole-dipole interaction. And in chapter 3 we move to laser cooling model, explaining more detail on resolved sideband cooling and its cooling efficiency, and how we simulate the steady-state phonon number. Then we present our finding in chapter 4, demonstrating our result on magic spacing and how it changes with dipole polarization as well as the effect of detuning and multiatom configuration on cooling performance. Finally we conclude in chapter 5.

Chapter2

Light-atom interaction

The interaction between light and atoms is a fundamental phenomenon in physics that has been extensively studied for decades [53]. It plays a crucial role in a wide range of fields, including quantum optics, atomic physics, and condensed matter physics [54]. In this chapter we will introduce the basic principles of the interaction, including the electric dipole approximation, the light-atom coupling and Markov approximation. And finally we will come to the core of this thesis, the photon-mediated dipole-dipole interaction [33]. This phenomenon arises when two electric dipoles, such as two atoms or molecules, interact with each other through the exchange of virtual photons. The photon-mediated dipole-dipole interaction can lead to a variety of interesting effects, such as long-range interactions between atoms, collective radiation behavior of dipole systems, and modifications of the spontaneous emission rate. These effects are particularly important in the study of quantum simulation and quantum computation, where the ability to control and manipulate the interaction between dipoles is essential. We will see these are also crucial for enhancing dark-state sideband cooling [1].

2.1 System of two level atoms and electric fields

We begin by considering a set of N indistinguishable atoms that are initially stationary in free space. Each atom is represented by a two-level system consisting of a ground state $|g\rangle$ and an excited state $|e\rangle$. The energy difference between these two states, which is equal to the resonant frequency of the atom, is denoted by $\hbar\omega$. Neglecting the zero-point energy, the Hamiltonian H_A that governs the dynamics of the atoms can be expressed as follows:

$$H_A = \sum_{\mu=1}^{N} \hbar\omega_0 \sigma_\mu^\dagger \sigma_\mu. \tag{2.1}$$

Here, the lowering operator for the μ-th atom is denoted by σ_μ, and is given by $\sigma_\mu = |g\rangle_\mu \langle e|_\mu$. Additionally, we assume that the transition dipole moment is real, and can be defined in terms of the lowering operator as follows $\hat{\mathbf{d}}_\mu = \mathbf{d}(\sigma_\mu + \sigma_\mu^\dagger)$ where **d** represents the magnitude and direction of the transition dipole moment.

In the meantime there is also quantized electromagnetic field modes in vacuum, defined by the field Hamiltonian H_F:

$$H_F = \sum_{\mathbf{k},s} \hbar\omega_{\mathbf{k}} a_{\mathbf{k}s}^\dagger a_{\mathbf{k}s}, \tag{2.2}$$

which sums over all possible wave vector **k** and polarization s. Here $a_{\mathbf{k}s}$ being annihilation operator of $\mathbf{k}s$' mode and $\hbar\omega_{\mathbf{k}} = \hbar c/|\mathbf{k}|$ is the corresponding energy. These operators relate to electric field operator $\mathbf{E}(\mathbf{r})$ on position $\mathbf{r}$. In the Coulomb gauge, the electric field

doi:10.6342/NTU202300902

can be written as

$$\mathbf{E}(\mathbf{r}) = \sum_{\mathbf{k},s} \sqrt{\frac{\omega_{\mathbf{k}}}{2\epsilon_0 \hbar V}} \hat{e}_{\mathbf{k}s} (a_{\mathbf{k}s} e^{i\mathbf{k}\cdot\mathbf{r}} + a_{\mathbf{k}s}^{\dagger} e^{-i\mathbf{k}\cdot\mathbf{r}}). \tag{2.3}$$

The interaction between light and matter in the presence of an electromagnetic field can be expressed as

$$H_{int} = -\mathbf{d} \cdot \mathbf{E}, \tag{2.4}$$

where **d** denotes the electric dipole moment. In the quantized version, the corresponding operators are used to express the interaction resulting in the Jaynes-Cummings interaction as follows:

$$H_{int} = -\hbar \sum_{\mathbf{k},s,\mu} g_{\mathbf{k}s} (\sigma_\mu + \sigma_\mu^{\dagger})(a_{\mathbf{k}s} e^{i\mathbf{k}\cdot\mathbf{r}_\mu} + a_{\mathbf{k}s}^{\dagger} e^{-i\mathbf{k}\cdot\mathbf{r}_\mu}). \tag{2.5}$$

The coupling constant $g_{\mathbf{k}s}$ is defined as $g_{\mathbf{k}s} = \sqrt{\frac{\omega_{\mathbf{k}}}{2\epsilon_0 \hbar^3 V}} (\hat{e}_{\mathbf{k}s} \cdot \mathbf{d})$, where $\omega_{\mathbf{k}}$ is the frequency of the electromagnetic mode, ϵ_0 is the vacuum permittivity, V is the quantization volume, $\hat{e}_{\mathbf{k}s}$ is the polarization vector of the photon.

2.2 Markov approximation for Open Quantum System

The Hamiltonian governing the interaction of atoms with light fields can be formulated, but solving for the exact dynamics becomes infeasible due to the infinite degrees of freedom in electromagnetic (EM) modes. Consequently, computationally representing the complete system-environment interaction becomes challenging. To address this challenge, one technique is to adopt the procedure in open quantum systems, whereby additional degrees of freedom are traced out, and the Markov approximation is used to derive an effective master equation. This equation is commonly referred to the Lindblad equation. By identifying the atom and field parts as the system H_S and environment H_B, respectively, we aim to determine the dynamics of the atom part $\rho_S(t)$ without the knowledge of the field. This can be accomplished by partially tracing over the full system and environment density, yielding $\rho_S = \mathrm{Tr}_B(\rho_S \otimes \rho_B)$.

In this section, we will explore how the same method can be applied to a system of a two-level atom interacting with electric fields. The goal is to derive an effective master equation for the atomic system without requiring knowledge of the field. By using the full Hamiltonian $H = H_A + H_F + H_{int}$, we obtain the operator's equation of motion in the Heisenberg picture [33]:

$$\frac{d}{dt}a_{\mathbf{k}s} = \frac{i}{\hbar}[H, a_{\mathbf{k}s}] = -i\omega_{\mathbf{k}}a_{\mathbf{k}s} + ig_{\mathbf{k}s}\sum_{\mu} s_{\mu}e^{-i\mathbf{k}\cdot\mathbf{r}_{\mu}}, \tag{2.6}$$

where the operator $\hat{s}_\mu$ is defined as $\hat{s}_\mu = \sigma_\mu + \sigma_\mu^\dagger$, and σ_μ is the lowering operator $\sigma_\mu = |g\rangle_\mu\langle e|_\mu$ for atom μ. The exact solution to this equation is:

$$a_{\mathbf{k}s}(t) = a_{\mathbf{k}s}(0)e^{-i\omega_{\mathbf{k}}t} + i\sum_{\mu} g_{\mathbf{k}s}e^{-i\mathbf{k}\cdot\mathbf{r}_{\mu}}\int_0^t dt'\hat{s}_\mu(t')e^{-i\omega_{\mathbf{k}}(t-t')}. \tag{2.7}$$

Similarly, for any atomic operator Q, we have:

$$\frac{d}{dt}Q = i\omega_0\sum_{\mu}[\sigma_\mu^\dagger\sigma_\mu, Q] - i\sum_{\mathbf{k},s,\mu} g_{\mathbf{k}s}[s_\mu, Q]\left(a_{\mathbf{k}s}e^{i\mathbf{k}\cdot\mathbf{r}_{\mu}} + a_{\mathbf{k}s}^\dagger e^{-i\mathbf{k}\cdot\mathbf{r}_{\mu}}\right). \tag{2.8}$$

Replacing $a_{\mathbf{k}s}e^{i\mathbf{k}\cdot\mathbf{r}_{\mu}}$ part with equation (2.7), its contribution in $\frac{d}{dt}Q$ becomes:

$$-i\sum_{\mathbf{k},s,\mu} g_{\mathbf{k}s}[\hat{s}_\mu, Q]a_{\mathbf{k}s}(0)e^{i(\mathbf{k}\cdot\mathbf{r}_{\mu}-\omega_{\mathbf{k}}t)} + \sum_{\mathbf{k},s,\mu,\nu} g_{\mathbf{k}s}^2 e^{i\mathbf{k}\cdot\mathbf{r}_{\mu\nu}}[\hat{s}_\mu, Q]\int_0^t dt'\hat{s}_\nu(t')e^{-i\omega_{\mathbf{k}}(t-t')}, \tag{2.9}$$

where $\mathbf{r}_{\mu\nu} \equiv \mathbf{r}_\mu - \mathbf{r}_\nu$ are defined as the position difference between atoms. The first term in equation (2.9) represents the contribution of initial field $\mathbf{E}_0 \equiv \mathbf{E}_0^+ + h.c.$ where:

$$\mathbf{E}_0^+(\mathbf{r},t) = \sum_{\mathbf{k},s} \sqrt{\frac{\omega_\mathbf{k}}{2\epsilon_0 \hbar^3 V}} \hat{e}_{\mathbf{k}s} a_{\mathbf{k}s}(0) e^{i(\mathbf{k}\cdot\mathbf{r}-\omega_\mathbf{k} t)}. \tag{2.10}$$

And thus we can use it to rewrite the first term in equation (2.9) that

$$-i\sum_\mu [\hat{s}_\mu, Q]\mathbf{E}_0^+ \cdot \mathbf{d} + \sum_{\mathbf{k},s,\mu,\nu} g_{\mathbf{k}s}^2 e^{i\mathbf{k}\cdot\mathbf{r}_{\mu\nu}}[\hat{s}_\mu, Q] \int_0^t dt' \hat{s}_\nu(t') e^{-i\omega_\mathbf{k}(t-t')}. \tag{2.11}$$

We can transform the infinite sum over EM modes $\mathbf{k}s$ into an integral by taking the continuum limit $V \to \infty$. In this case, we obtain

$$\lim_{V\to\infty} \frac{1}{V} \sum_{\mathbf{k},s} (\hat{e}_{\mathbf{k}s}\cdot\mathbf{d})^2 e^{i\mathbf{k}\cdot\mathbf{r}_{\mu\nu}} = (2\pi c)^{-3} \int_0^\infty \omega^2 d\omega \int d\Omega \sum_s (\hat{\Omega}_s \cdot \mathbf{d})^2 e^{i\omega d\hat{\Omega}\cdot\mathbf{r}_{\mu\nu}/c}, \tag{2.12}$$

where $d\hat{\Omega}$ and $\hat{\Omega}_s$ are the normal vector and tangent space basis vector on the small surface $d\Omega$, respectively. In Euclidean space, we can evaluate this angular integral straightforwardly since $\hat{\Omega}_s$ and $d\hat{\Omega}$ form a complete basis. Hence, we obtain:

$$\sum_s (\hat{\Omega}_s \cdot \mathbf{d})^2 = d^2(1 - (d\hat{\Omega}\cdot\hat{\mathbf{d}})^2). \tag{2.13}$$

Using above result, equation (2.11) in the continuum limit becomes:

$$-i\sum_\mu [\hat{s}_\mu, Q]\mathbf{E}_0^+ \cdot \mathbf{d} + \sum_{\mu\nu} \frac{d^2}{16\epsilon_0 \pi^2 \hbar^3 c^3}[\hat{s}_\mu, Q]$$

$$\times \int d\Omega (1 - (d\hat{\Omega}\cdot\hat{\mathbf{d}})^2) \int_0^\infty d\omega \omega^3 e^{i\omega d\hat{\Omega}\cdot\mathbf{r}_{\mu\nu}/c} \int_0^t dt' \hat{s}_\nu(t') e^{i\omega(t'-t)}. \tag{2.14}$$

In order to derive a solvable master equation, it is necessary to address the dependence of the integrand in equation (2.14) on the past history of the operator $\hat{s}_\nu$. To this end, the Markov approximation can be employed. This approximation assumes that the system-environment interaction is weak, and that the environment relaxes quickly compared to the dynamics of the system. Under this assumption, the correlation time of the environment is much shorter than the typical time scale of the system's evolution, allowing for a memoryless (Markovian) approximation of the system's time evolution. In this approximation, the past operator can be treated as non-interacting, and is therefore simply replaced with a current operator plus an oscillating phase. Specifically, we replace $\hat{s}_\nu(t')$ in equation (2.14) with:

$$\hat{s}_\nu(t') \to \sigma_\nu(t) e^{-i\omega_0(t'-t)} + h.c. \tag{2.15}$$

After this, the dependence of t still remains in equation (2.14). To achieve a time-independent interaction by eliminating time dependence, we note that the timescale of interest is much larger than the resonance period, $\omega_0 t \gg 1$, since for typical two-level atoms like rubidium-87, the transition frequency between $5S_{1/2}$ and $5P_{1/2}$ is approximately 377 THz while the experimental time scale is around MHz order. Therefore, it is valid to set t to infinity, and this approximation still yields a finite result and is a safe one.

In summary, original integral in equation (2.14) reduces to a solvable form:

$$\int d\Omega (1 - (d\hat{\Omega} \cdot \hat{\mathbf{d}})^2) \int_0^\infty d\omega \omega^3 e^{i\omega d\hat{\Omega} \cdot \mathbf{r}_{\mu\nu}/c} \int_0^\infty dt \left[\sigma_\nu e^{-i(\omega-\omega_0)t} + \sigma_\nu^\dagger e^{-i(\omega+\omega_0)t} \right]. \tag{2.16}$$

2.3 Photon-mediated dipole-dipole interaction

In Section 2.2 of the present work, we derive the effective equation of motion for the photon-mediated dipole-dipole interaction between two-level atoms in a Markovian approximation. The calculation of equation (2.14) is presented in Appendix A. We employ the rotating-wave approximation to arrive at the Lindblad equation in the density matrix

doi:10.6342/NTU202300902

representation, which takes the form:

$$\dot{\rho} = -i[H,\rho] - i\sum_{\mu\neq\nu} g_{\mu\nu}[\sigma_\mu^\dagger\sigma_\nu,\rho] + \sum_{\mu\nu}\gamma_{\mu\nu}\mathcal{L}_{\mu\nu}[\rho]. \tag{2.17}$$

The above Lindblad map is defined by $\mathcal{L}_{\mu\nu}[\rho] = \sigma_\nu\rho\sigma_\mu^\dagger - \frac{1}{2}\{\sigma_\mu^\dagger\sigma_\nu,\rho\}$, while the term involving different atomic operator $\sigma_\mu^\dagger\sigma_\nu$ represents the well-known photon-mediated dipole-dipole interaction or resonant dipole-dipole interaction (RDDI), which arises from the photon-mediated coupling between the atomic dipoles. The collective energy shift $g_{\mu\nu}$ and collective decay $\gamma_{\mu\nu}$ are described by the second and third terms in the equation, respectively. The parameters $g_{\mu\nu}$ and $\gamma_{\mu\nu}$ depend on the distance between the atoms and the polarization angle of their dipole moments, given by $\xi = k|\vec{s}_{\mu\nu}| \equiv k|\vec{r}_\mu - \vec{r}_\nu|$ and $\cos\theta \equiv \hat{\mathbf{d}}\cdot\hat{s}_{\mu\nu}$, where $\hat{\mathbf{d}}$ is the unit vector of polarization. The explicit expressions for $\gamma_{\mu\nu}$ and $g_{\mu\nu}$ are given by:

$$g_{\mu\nu} = \frac{3\Gamma}{4}\left\{-[1-\cos^2\theta]\frac{\cos\xi}{\xi} + [1-3\cos^2\theta]\left[\frac{\sin\xi}{\xi^2} + \frac{\cos\xi}{\xi^3}\right]\right\}, \tag{2.18}$$

$$\gamma_{\mu\nu} = \frac{3\Gamma}{2}\left\{[1-\cos^2\theta]\frac{\sin\xi}{\xi} + [1-3\cos^2\theta]\left[\frac{\cos\xi}{\xi^2} - \frac{\sin\xi}{\xi^3}\right]\right\}. \tag{2.19}$$

The diagonal term of the collective decay, $\gamma_{\mu\mu}$, is identified as the single atom spontaneous decay rate, denoted as Γ. Figure 2.1 shows the values of $\gamma_{\mu\nu}$ and $g_{\mu\nu}$ for different polarization angles $\cos\theta$ and atomic spacings ξ.

In the field of quantum information processing, photon-mediated dipole-dipole interactions have been proposed as a means of implementing quantum gates and entangling operations in atomic ensembles [55]. Additionally, photon-mediated dipole-dipole interactions have been studied in solid-state systems such as semiconductor quantum dots, where they can be used to control and manipulate the spin states of individual excitons

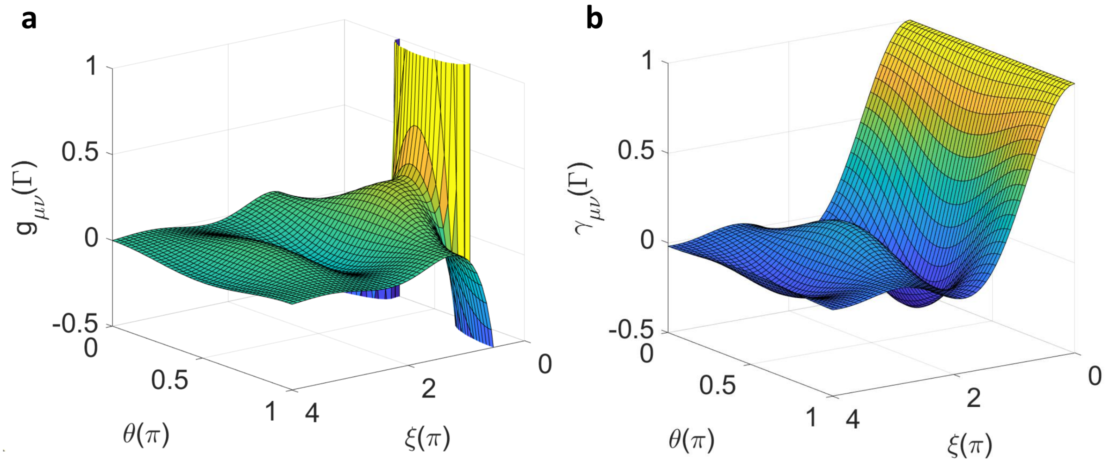

Figure 2.1: Collective energy shift $g_{\mu\nu}$ (a) and decay rate $\gamma_{\mu\nu}$ (b) under various polarization angles $\cos\theta$ and atomic spacings ξ. The collective decay rate $\gamma_{\mu\nu}$ approaches single atom decay rate Γ while energy shift $g_{\mu\nu}$ diverges in short distance limit $\xi \rightarrow 0$.

[56].

In chirally coupled waveguides, the same interactions can be used for efficient cooling of atomic motion to the ground state [37]. Chirally coupled waveguides involve the asymmetric coupling of photon modes, leading to the emergence of nonreciprocal photon-mediated dipole-dipole interactions. By adjusting the strength of the nonreciprocal coupling, the interaction between the counterpropagating modes can be tuned to cool the motion of the atom more efficiently than conventional cooling methods. This cooling technique is highly efficient and can be used to prepare the atom close to its motional ground state, which is important for various quantum computation tasks.

In summary, photon-mediated dipole-dipole interactions are a powerful tool for controlling and manipulating the quantum properties of atoms and molecules, with potential applications in quantum computations. Later, we will explore the use of these interactions to enhance cooling efficiency and achieve lower temperatures than with conventional cooling methods without assistance of RDDIs.

Chapter3

Resolved sideband cooling

Resolved sideband cooling is a powerful technique used in quantum optics and quantum simulation to cool individual atoms or ions down to their motional ground state [23]. It involves coupling the internal states of the atom or ion with its motional states through laser light, such that the energy of the internal state changes with the motional state of the particle. By exciting these internal states using laser light followed by spontaneous emissions, the particle's motional energy can be reduced, leading to cooling. Resolved sideband cooling has become a cornerstone of many quantum technologies, enabling precise control of atomic and ionic motion and paving the way for advances in quantum computing and simulation [10, 15].

On the other hand, the dark-state sideband cooling method [27, 39, 57] is a cooling technique utilized in ultracold atoms that employs a Λ-type three-level configuration of atoms, with two laser fields acting on two distinct hyperfine ground states sharing one common excited state. Through quantum interference between the two ground states, an effective dark-state picture is formed. Under proper parameter setup, this configuration results in the formation of an asymmetric absorption profile, allowing for the cooling of atoms by removing one phonon via a transition in the resolved sideband. This technique is similar to the conventional resolved sideband cooling technique that operates on two-level ions, but with adjustable effective laser driving and decay rates. Due to the adaptability of the effective parameters in dark-state sideband cooling, it becomes a versatile and commonly used cooling technique for neutral atoms [31, 58].

The objective of this section is to explore the fundamental principles underlying the resolved sideband cooling and dark-state cooling techniques. This exploration will provide us with a comprehensive understanding of the principles essential for studying the main topic of this thesis, namely, the influence of dipole-dipole interactions in dark-state cooling. Furthermore, in addition to presenting our results in Chapter 4, we will also outline our numerical approach and describe our methodology for determining the cooling efficiency.

3.1 Atomic motion and sideband

In the field of quantum optics, understanding and controlling the motion of individual atoms and ions is crucial for the development of many quantum technologies. Atomic motion is typically characterized by its frequency or energy, which can be quantized into a set of discrete levels. In certain cases, the internal states of an atom or ion can be associated with its motion, leading to a phenomenon known as a ”sideband”. A sideband occurs when the energy of the internal states of the atom or ion changes as a result of its motion. For example, if an atom or ion in a harmonic trap is carrying some motional quanta, then the energy of its internal states can be shifted by an amount proportional to that motional quanta frequency. This shift can be detected and controlled using laser light, allowing

doi:10.6342/NTU202300902

researchers to manipulate the motion of individual particles with remarkable precision.

An atom confined in a small region experiences a potential that can be approximated by a 3-dimensional quadratic potential. Under this potential, the atom's motional Hamiltonian can be expressed as:

$$H_{motion} = \sum_{i=1}^{3} \frac{\hat{p}_i^2}{2m} + \frac{m\nu_i^2}{2}\hat{r}_i^2, \tag{3.1}$$

such that $\hat{p}_i, \hat{r}_i$ are momentum and position operators on ith direction respectively while ν_i is the oscillation frequency on that direction. m is the mass of the atom. The dynamics of the atom under this potential can be described using creation and annihilation operators $\hat{a}_\mu, \hat{a}_\mu^\dagger$ corresponding to the motional modes (phonons). Additionally, operators $\hat{r}_i$, $\hat{p}_i$ are related to the creation and annihilation operators as follows:

$$\hat{r}_i = \frac{1}{\sqrt{2m\nu_i}}(\hat{a}_i + \hat{a}_i^\dagger), \tag{3.2}$$

$$\hat{p}_i = i\sqrt{\frac{m\nu_i}{2}}(\hat{a}_i - \hat{a}_i^\dagger). \tag{3.3}$$

For simplicity, we consider only one-dimensional motional mode and include the internal energy discussed in equation (2.1) to obtain the full Hamiltonian ($\hbar = 1$):

$$H = H_A + H_{motion} = \omega_0\sigma^\dagger\sigma + \nu a^\dagger a. \tag{3.4}$$

The eigenstates of the Hamiltonian depend on the internal state (ground or excited) of the atom and the number of phonons it carries, i.e., $|a, n\rangle$, where $a \in \{e, g\}$ and $n \in \mathbb{N}$.

These energy levels that arise due to the coupling between the internal states of an

doi:10.6342/NTU202300902

atom or ion and its motion in a trap results in an equally spaced sideband spectrum [59]. When a laser is tuned to a frequency that corresponds to the energy difference between two internal states ($|e, n\rangle \leftrightarrow |g, n\rangle$), it can induce transitions between those states by absorbing or emitting a photon. However, if the frequency of the laser is not exactly equal to the energy difference between the two states, but instead is slightly detuned, then the absorption or emission of the photon will not only change the internal state of the atom, but will also excite or de-excite its motion in the trap. This results in the appearance of sidebands in the spectrum of the absorbed or emitted light, corresponding to the different possible motional states of the particle.

3.2 Lamb-Dicke regime

Now that we have established the energy level structure of trapped atoms, we can delve deeper into their interaction with an external classical standing wave driving field, $-\mathbf{E}_0 \sin(kx)$, which we have transformed into a rotating frame. The atom is placed at the node of the driving field, and we are interested in understanding the interaction between the light and the atom's x-direction motional mode. This interaction can be described by using Equation (2.4), with all classical numbers replaced by quantum operators:

$$H_{int} = \frac{\Omega}{2}(\sigma + \sigma^\dagger)\sin(k\hat{x}) = \frac{\Omega}{2}(\sigma + \sigma^\dagger)\sin\left(\frac{k}{\sqrt{2m\nu}}(\hat{a} + \hat{a}^\dagger)\right), \tag{3.5}$$

where the Rabi frequency is given by $\Omega/2 = \mathbf{d} \cdot \mathbf{E}_0$ and k is the wave vector of laser pumping.

In atomic physics, the Lamb-Dicke regime is a condition where the amplitude of an atom's motion is significantly smaller compared to the wavelength of the laser used to

doi:10.6342/NTU202300902

interact with it. This can be expressed mathematically as $k^2\langle \hat{x} \rangle^2 \ll 1$, or equivalently [60]:

$$\eta^2(2\langle n \rangle + 1) \ll 1, \tag{3.6}$$

where $\eta = \frac{k}{\sqrt{2m\nu}}$ is the Lamb-Dicke parameter that characterizes the strength of the interaction between the laser and the atomic motion, and $\langle n \rangle$ is the average number of phonons in the motional mode of the atom.

When the parameter η is much smaller than 1, the condition in equation (3.5) is automatically satisfied for any state. In this case, the sine function in equation (3.4) can be expanded to the first order, yielding the approximate interaction Hamiltonian given by:

$$H_{int,LD} \approx \frac{\eta\Omega}{2}(\sigma + \sigma^\dagger)(\hat{a} + \hat{a}^\dagger). \tag{3.7}$$

In the Lamb-Dicke regime, it is possible to selectively manipulate the internal states of an atom or ion by tuning the coupling strength $\eta\Omega$. This regime is particularly important for various applications in quantum computation and quantum simulation, as it enables precise control of the atomic motion and its interaction with the laser.

Experimentalists can achieve the Lamb-Dicke regime by trapping the particle in a trap with a high confinement strength ν, such as a radiofrequency (RF) trap or a magnetic trap. This regime is a crucial regime of atomic motion that enables precise manipulation of atomic internal states with laser light. This regime plays a central role in many areas of quantum physics, and is also important to make the resolved sideband cooling work, in which one needs to control the transition between two specific states.

3.3 Dark-state sideband cooling

To cool individual particles to their motional ground state, one widely-used technique is resolved sideband cooling. It is a technique that relies on this sideband interaction to cool individual particles to their motional ground state. By exciting the internal states of an atom or ion with laser light, the particle's motional energy can be reduced through spontaneous emission, ultimately leading to its cooling.

To illustrate this technique, let us consider a single atom in free space driven by a standing wave laser [23], where we focus solely on the motion of the atom along the x-direction, which couples with the laser. Using equations (2.17) and (3.6), we obtain the master equation:

$$\dot{\rho} = -i[H_{LD}, \rho] + \Gamma \left(\sigma \rho \sigma^\dagger - \frac{1}{2}\{\sigma^\dagger \sigma, \rho\} \right). \tag{3.8}$$

Here, Γ represents the damping rate of the system due to spontaneous emission and H_{LD} is the Hamiltonian in the Lamb-Dicke regime:

$$H_{LD} = -\Delta \sigma^\dagger \sigma + \nu \hat{a}^\dagger \hat{a} + \frac{\eta \Omega}{2}(\sigma + \sigma^\dagger)(\hat{a} + \hat{a}^\dagger). \tag{3.9}$$

In the context of a two-level atom with energy levels $|n\rangle$ of energies $(n + 1/2)\nu$ and spontaneous decay rate Γ, a laser with Rabi frequency Ω is applied with detuning $\Delta = \omega - \omega_0$. In the Lamb-Dicke regime with LD parameter $\eta \ll 1$, this induces a red sideband transition $|g, n\rangle \leftrightarrow |e, n-1\rangle$ and a blue sideband transition $|g, n\rangle \leftrightarrow |e, n+1\rangle$ with strengths $\eta\Omega\sqrt{n}$ and $\eta\Omega\sqrt{n+1}$, respectively.

When a standing wave laser is applied, the carrier transition $|g, n\rangle \leftrightarrow |e, n\rangle$ is immediately eliminated as we observe from the interaction form in equation (3.9). An atom in the excited state $|e, n\rangle$ decays to the ground state at a rate Γ due to the interaction with the vacuum EM mode. By maximizing the red sideband transition rate, cooling can be achieved through the process $|g, n\rangle \rightarrow |e, n-1\rangle \rightarrow |g, n-1\rangle$, and so on, down to the motional ground state. Two additional conditions are necessary for this process: first, the laser must be tuned to the red sideband resonance by setting $\Delta = -\nu$, and second, the resolved sideband condition $\Gamma \ll \nu$ must be satisfied to make the blue sideband transition far-detuned and almost negligible compared to the red sideband transition. Using these conditions, we can calculate that resolved sideband cooling reduces the phonon number to approximately [57] $\langle n\rangle \approx \frac{\eta^2\Omega^2}{8\nu^2} + \frac{\Gamma^2}{16\nu^2}$. The first term comes from finite driving strength that heats the atom. The second term is due to non-vanishing blue sideband transition rate relating to absorption width Γ, which exists even in weak driving limit $\eta\Omega \rightarrow 0$.

One potential limitation of standing wave sideband cooling is that it may not be easy to implement a standing wave laser. Additionally, the natural linewidth Γ is not a tunable parameter, so the resolved sideband condition $\Gamma \ll \nu$ may not be satisfied. To address these limitations, the dark-state cooling scheme was developed [57].

This cooling scheme is based on the conventional EIT cooling scheme, which requires a Λ-type atomic structure with two ground states $|g\rangle$ and $|r\rangle$ sharing the same excited state $|e\rangle$, and is driven by two lasers with Rabi frequencies being Ω_g and Ω_r. The EIT Hamiltonian can be written using equation (3.4):

$$H_{EIT} = -\Delta\sigma_g^\dagger\sigma_g + \nu a^\dagger a + \frac{\Omega_g}{2}(\sigma_g e^{-ik_g\hat{x}} + \sigma_g^\dagger e^{ik_g\hat{x}}) + \frac{\Omega_r}{2}(\sigma_r e^{-ik_r\hat{x}} + \sigma_r^\dagger e^{ik_r\hat{x}}), \quad (3.10)$$

where k_g and k_r are corresponding wave vector to the two laser driving. In Λ-type structure the transition between $|r\rangle \rightarrow |g\rangle$ is forbidden. Referring to the derivation in section 2, we can obtain a master equation that incorporates two dissipation processes: $|e\rangle \rightarrow |g\rangle$ and $|e\rangle \rightarrow |r\rangle$:

$$\dot{\rho} = -i[H_{EIT}, \rho] + \gamma_g \left(\sigma_g \rho \sigma_g^\dagger - \frac{1}{2}\{\sigma_g^\dagger \sigma_g, \rho\} \right) + \gamma_r \left(\sigma_r \rho \sigma_r^\dagger - \frac{1}{2}\{\sigma_r^\dagger \sigma_r, \rho\} \right), \tag{3.11}$$

where $\sigma_g \equiv |g\rangle\langle e|$, $\sigma_r \equiv |r\rangle\langle e|$. And γ_g, γ_r are corresponding decay rate. Both lasers are set to have a common detuning Δ. We can expand the Hamiltonian with respect to the Lamb-Dicke parameter $\eta_g = k_g/\sqrt{2m\nu}$ and $\eta_r = k_r/\sqrt{2m\nu}$. For zeroth-order expansion of the Hamiltonian with respect to both Lamb-Dicke parameters η_g and η_r, we can diagonalize it into [57]:

$$\begin{aligned} |+\rangle &= \sin\phi|e\rangle - \cos\phi(\sin\theta|g\rangle + \cos\theta|r\rangle), \\ |-\rangle &= \cos\phi|e\rangle + \sin\phi(\sin\theta|g\rangle + \cos\theta|r\rangle), \\ |d\rangle &= \cos\theta|g\rangle - \sin\theta|r\rangle. \end{aligned} \tag{3.12}$$

The energy eigenvalues are $\omega_\pm = \frac{1}{2}\left(-\Delta \pm \sqrt{\Delta^2 + \Omega_r^2 + \Omega_g^2}\right)$, $\omega_d = 0$. The angle θ and ϕ are defined as

$$\theta = \tan^{-1}\frac{\Omega_g}{\Omega_r}, \tag{3.13}$$

$$\phi = -\frac{1}{2}\tan^{-1}\frac{\sqrt{\Omega_r^2 + \Omega_g^2}}{\Delta^2}. \tag{3.14}$$

In typical setting, large values of detuning Δ and Rabi frequency Ω_r are employed to minimize both angles. Consequently, the dark state becomes highly similar to the ground state $|d\rangle \approx |g\rangle$, allowing for the preparation of a dark state by initially placing the atom in the ground state $|g\rangle$.

In the first order expansion of η_g and η_r, we express the Hamiltonian in the same basis as before:

$$H^{(1)} = \left[\frac{i\eta_-}{2}\Omega^+ \sin\phi|d\rangle\langle+| + \frac{i\eta_-}{2}\Omega^+ \cos\phi|d\rangle\langle-| + \frac{i\eta_+}{2}\Omega^+|-\rangle\langle+|\right](a + a^\dagger) + h.c., \tag{3.15}$$

where $\eta_\pm = \eta_g \pm \eta_r$ and $\Omega^+ = \frac{\Omega_g\Omega_r}{\sqrt{\Omega_r^2+\Omega_g^2}} \sin\phi$. By appropriately choosing the detuning Δ, the Rabi frequencies Ω_g and Ω_r, we can make $\omega_+ = \nu$ such that the effective red sideband transition $|d, n\rangle \to |+, n-1\rangle$ is resonant, while the other state $|-\rangle$ is far-detuned and can thus be neglected. This effectively reduces the Λ-type system to a two-level system, allowing us to use the results we have discussed earlier. In this two-level basis, the spontaneous decay rate becomes:

$$\gamma_{\text{eff}} = \frac{\sin^2\phi}{2}(\gamma_g \cos^2\theta + \gamma_r \sin^2\theta) \tag{3.16}$$

and the effective LD parameter η_{eff} and Rabi frequency Ω_{eff} are given by $\eta_{\text{eff}} = \eta_-$ and $\Omega_{\text{eff}} = \Omega^+$ as shown in (3.14). In order to achieve high cooling efficiency, it is necessary to make all of these parameters small while keeping $\omega_+ = \nu$. In practice, this can be achieved by ensuring that Ω_g is much smaller than both Ω_r and Δ, that is, $\Omega_g \ll \Omega_r \ll \Delta$.

We can see that dark-state sideband cooling presents several advantages over traditional resolved cooling techniques. Unlike the two-level structure, the tunable effective parameters in this cooling scheme make it more flexible to apply in experiments. These tunable parameters enable faster cooling rates, higher cooling efficiencies, and reduced sensitivity to experimental imperfections. Consequently, it has been implemented in various experimental settings [27, 58, 61–68] to cool individual atoms and ions to their motional ground state. In this thesis, we work with the dark-state cooling scheme due to its more flexible parameter choices, making it more convenient for us to explore various regions within experimental feasibility.

3.4 Simulating method

We will now extend to a system of N two-level trapped atoms that are driven by standing wave lasers. As previously discussed, this system can be cooled using the dark-state sideband cooling technique with Λ-type atoms driven by two laser fields. We assume that the atoms are trapped in a one-dimensional harmonic potential, where the trapping frequency is ν. We further assume that this trap potential is the weakest trapped direction compared to the other motional modes. The effective two-level system for the μth atom is denoted as $|g\rangle_\mu$ and $|e\rangle_\mu$.

In the LD regime, the LD parameter is defined as $\eta = \frac{k_{\text{eff}}}{\sqrt{2m\nu}}$, where m is the atom mass and k_{eff} the effective wave vector. The system Hamiltonian can be written as follows:

$$H_{LD} = -\Delta \sum_{\mu=1}^{N} \sigma_\mu^\dagger \sigma_\mu + \nu \sum_{\mu=1}^{N} a_\mu^\dagger a_\mu + \frac{\eta}{2} \sum_{\mu=1}^{N} \Omega_\mu (\sigma_\mu^\dagger + \sigma_\mu)(a_\mu^\dagger + a_\mu). \tag{3.17}$$

Here the lowering operator $\sigma_\mu = |g\rangle_\mu \langle e|$ acts on the μth atom, while the annihilation operator a_μ acts on the phonon mode associated with the same atom. The position-dependent Rabi frequency is given by Ω_μ, which carries an atomic label. The detuning $\Delta = \omega_L - \omega_0$ represents the difference between the central frequency of the laser and the atomic transition frequency.

When this collection of atoms is placed in vacuum, the system dynamics can be mod-

doi:10.6342/NTU202300902

eled using a master equation that takes into account dipole-dipole interactions:

$$\dot{\rho} = -i[H_{LD}, \rho] - i \sum_{\substack{\mu,\nu=1 \\ \mu\neq\nu}}^{N} g_{\mu\nu}[\sigma_\mu^\dagger \sigma_\nu, \rho] + \sum_{\mu,\nu=1}^{N} \gamma_{\mu\nu}\mathcal{L}_{\mu\nu}[\rho]. \tag{3.18}$$

The energy shift $g_{\mu\nu}$ and collective decay rate $\gamma_{\mu\nu}$, which have been defined previously, are dependent on the atoms' spacings, denoted by $\xi = k|\vec{s}_{\mu\nu}| = k|\vec{r}_\mu - \vec{r}_\nu|$ with $k = 2\pi/\lambda$ and the laser transition wavelength λ, as well as the dipole polarization angle $\cos\theta = \hat{\mathbf{d}} \cdot \hat{s}_{\mu\nu}$, where $\hat{\mathbf{d}}$ is the unit vector of polarization. These factors play a crucial role in determining the strength of the energy shift and collective decay rate.

In general, the state space of the density matrix ρ includes a tensor product of finite spin states and infinite-dimensional Fock states. To address this issue, we introduce a phonon cutoff number $n_c = 1$, such that the density matrix only contains atom states with a phonon number no greater than n_c, reducing the state space to a finite dimension. This is valid, in particular, when the steady-state phonon number $\langle n_\mu \rangle = \mathrm{tr}(a_\mu^\dagger a_\mu \rho_{st}) \ll 1$ is much less than one, where ρ_{st} satisfies $\dot{\rho}_{st} = 0$. This is commonly observed as the resolved sideband condition is satisfied.

By using this truncation, one can numerically solve for the steady-state density matrix via equation (3.17). For a system of N atoms, where each atom has four internal states $|g(e), 0(1)\rangle$, the state space has dimension 4^N, and the density matrix has thus 4^{2N} elements. To perform calculations, we transform the full master equation (3.17) into Liouville-Fock space and search for its null space. However, the computational cost increases exponentially with a rate of 4^{6N}. This limits our ability to study exact properties of large atom systems, and our discussion is limited to a few atoms (up to 5). Nevertheless, in the next chapter, we show that even for a few atoms (even just two atoms), dipole-dipole

doi:10.6342/NTU202300902

interactions can still play an important role and significantly affect cooling efficiency.

Chapter4

Enhancing sideband cooling via dipole-dipole interaction

In this section, we present our primary findings concerning the utilization of resonant dipole-dipole interactions for enhanced cooling performance. Firstly, we demonstrate the existence of the magic spacing in the case of two and three atoms, which results in enhanced cooling performance. Subsequently, we search on other magic spacings contributing to superior cooling as a consequence of variations in light polarization orientations. We then investigate the impact of laser detuning and multi-atom configurations. Our analysis shows that, compared to the single-atom case, a reduction in phonon occupations of up to 13-17% can be achieved in our investigations, thereby demonstrating the potential of RDDIs for cooling free-space atoms beyond single-atom limits. We note that decreasing the driving strength improves performance, but the cooling rate will be sacrificed due to weak driving.

The emergence of enhanced cooling through resonant DDIs, which causes reabsorption of light, is a unique feature compared to conventional laser cooling techniques and

doi:10.6342/NTU202300902

magneto-optical traps. This is due to the asymmetric driving conditions and the identification of magic atomic spacings that involve spectator atoms. These spectator atoms act as a coolant and absorb phonons of the target atom which is driven more intensely than the spectator atoms. But in the same time, since the RDDIs are reciprocal, they can emit the phonons back to the target atom and heat it up through spin-exchange interaction. The asymmetric driving field can suppress the latter process and removes more heat than that returned from the RDDIs, enhancing the cooling performance in given parameter setup. However, it should be noted that the reabsorption process does not always result in superior cooling.

We will show that when the atoms are in close proximity, strong DDIs can result in multiple scattering that heats up the target atom. It is important to note that in our analysis, we assume that the system is in the LD regime, where all atoms are close to their motional ground. This assumption holds true under the condition that all atoms have undergone precooling using conventional dark-state sideband cooling methods. The key factor here is that, by employing asymmetric driving conditions, the target atom can be cooled beyond the single-atom limit, reaching the motional ground state. This highlights the crucial role of spectator atoms in effectively transferring or extracting additional heat, surpassing the reabsorption process caused by RDDIs, especially when interparticle distances are set close to the optimal magic spacings.

4.1 Few atoms cases

We initially focus on two- and three-atom systems where one atom is the target while the others act as spectators or refrigerants. As illustrated in Fig. 4.1, the spectator atoms

doi:10.6342/NTU202300902

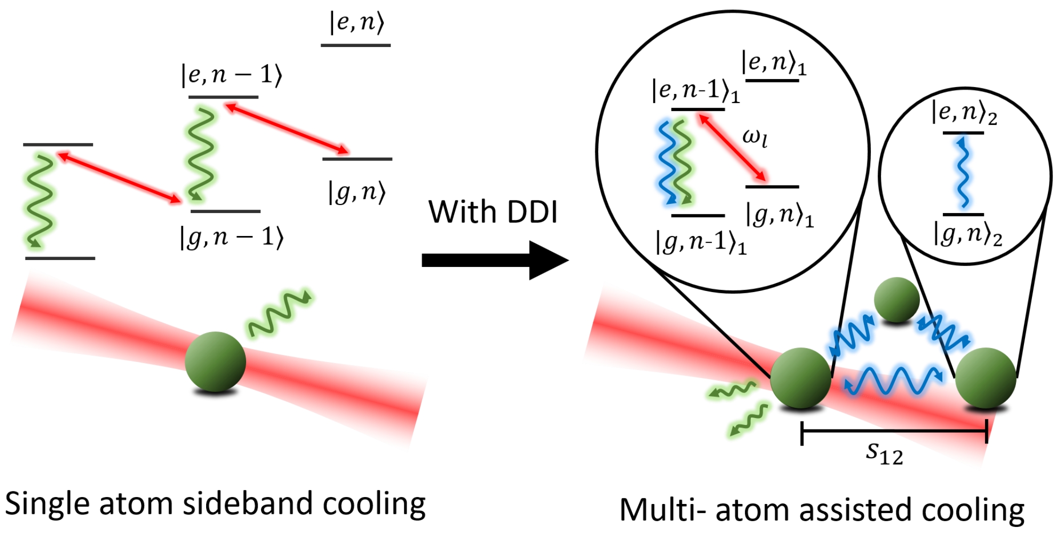

Figure 4.1: A diagram illustrating the multi-atom enhanced sideband cooling mechanism utilizing RDDIs within an equilateral triangle configuration with an interparticle spacing denoted as s_{12}. A laser (indicated by the red beam and arrow) is directed at the target atom. This laser drives the red-sideband transition from state $|g, n\rangle$ to $|e, n-1\rangle$, cooling the atom towards state $|g, n-1\rangle$ through the process of spontaneous emission(indicated by green arrow). The spin-exchange interactions in RDDIs (blue arrow) flip the spins of other atoms via multiple light scatterings while conserving atomic excitation numbers. The remaining spectator atoms can act as coolants, which extracts excess heat from the target atom through RDDIs, providing a special cooling mechanism. The figure has been adapted from [1]. Permission to adapt granted by the authors.

play the role of quantum emitters that enable collective spin-exchange interactions. By considering an asymmetric driving setup, such that the laser field only stimulates target atom (i.e., $\Omega_\mu = \Omega\delta_{\mu 1}$ in equation (3.16)), we can disregard the motional degrees of freedom of the other atoms and solely focus on the target atom's phononic degrees of freedom since the spectator's motional state will not couple to its spin for η order interaction in equation (3.17). As a result, the size of the spin-phonon spaces in equation (3.17) is greatly reduced. This approach of asymmetric driving has been investigated in the case of ion sideband cooling [37] and EIT cooling of neutral atoms in atom-waveguide interfaces [39]. It enables the exploration of new parameter ranges that can lead to enhanced cooling performance surpassing the limitations of cooling a single atom alone.

We start by computing the steady-state solutions of the target atom phonon num-

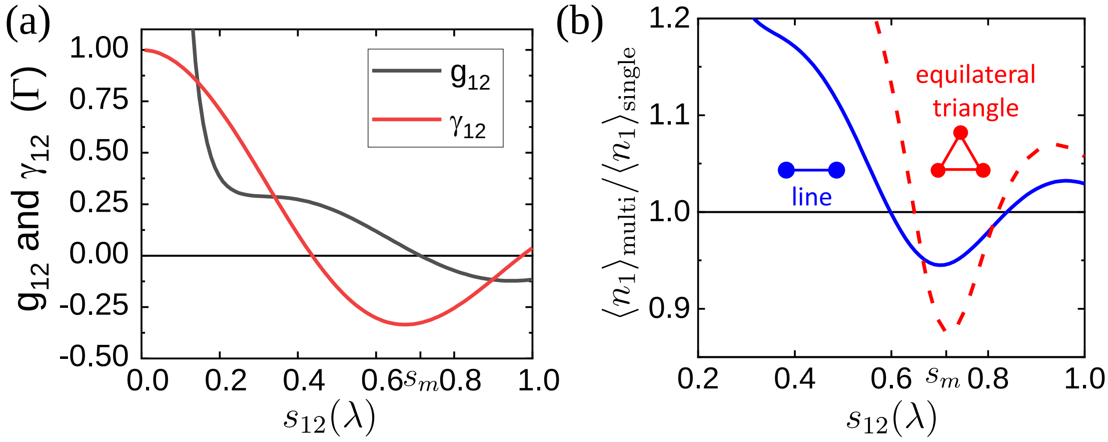

Figure 4.2: Enhanced sideband cooling and the determination of magic spacing for two- and three- atom's configurations. (a) depicts the collective frequency shift g_{12} and decay rate γ_{12} with polarization angle being perpendicular $\cos\theta = 0$, as a function of the atomic separation s_{12}, for several values within the range of λ. A vanishing g_{12} indicates the presence a magic spacing $s_m \approx 0.7133\lambda$. (b) shows the ratio of the phonon number of the target atom, $\langle n_1\rangle_{multi}$ to the single atom's limit, $\langle n_1\rangle_{single}$, in a multi-atom configuration, for atoms arranged in a line (indicated by blue-solid line) and an equilateral triangle shape (indicated by red-dashed line), as a function of s_{12} within λ. The sideband cooling parameters are set such that $\Delta = -\nu$, $\Gamma = 0.1\nu$, and $\eta\Omega_1 = 0.04\nu$. A maximal enhancement of cooling performance occurs at $s_{12} = s_m$. The figure has been adapted from [1]

ber in a multiatom system with RDDIs using equation (3.17) and setting $n_c = 1$. This choice of truncation number is sufficient in the LD regime and is confirmed to be convergent for higher n_c. The results are normalized with respect to the single atom value $\langle n_1\rangle_{single} = \frac{\eta^2\Omega^2}{8\nu^2} + \frac{\Gamma^2}{16\nu^2}$ [57] without RDDIs. The ratio $\langle n_1\rangle_{multi}/\langle n_1\rangle_{single}$ indicates the extent of cooling enhancement, with values below one indicating enhanced cooling behavior. In Figure 4.2(a), we determine the magic spacing for the two-atom scenario, which corresponds to the maximal enhancement of sideband cooling. We locate the magic interparticle distance, denoted as $s_m \approx 0.71\lambda$, in the case of perpendicular polarization, where the collective frequency shift g_{12} almost vanishes.

The identification of magic spacings can be understood by the interplay between a finite decay rate and a vanishing g_{12}. This regime allows for an additional γ_{12} to dissipate heat from individual atoms via collective spin-exchange coupling. By utilizing asymmetric driving with the magic spacing condition, more heat can be transferred from the target atom to the spectator atoms. Conversely, if $|g_{12}|$ increases and becomes non-zero shown in Fig. 4.2(a), the efficiency of spin-exchange interaction for spectator atoms to absorbing heat diminishes, leading to heating effects.

The absence of a collective frequency shift g_{12} observed in our study is similar to the cooling condition observed at $\xi = 0, \pi$ in the context of exp$(i\xi)$ [37, 39]. This similarity arises due to the spatial characteristics of an long-range photon-mediated dipole-dipole interaction within a one-dimensional atom-waveguide platform [69, 70]. At s_m, when γ_{12} is finite and $|\gamma_{12}| < \Gamma$, as indicated in Fig. 4.2(a), this condition allows for access to cooling regimes similar to those observed in an atom-waveguide system with reciprocal couplings to non-guided modes. These regimes can be precisely quantified as $\gamma_{non} = (\Gamma - |\gamma_{12}|)$ [37].

In Fig. 4.2, we note that the magic spacing will result in a local minimum γ_{12}. When considering various light polarizations that is not perpendicular $\theta \neq \pi/2$ and in the short distance regime, additional magic spacings appear at a vanishing g_{12} but with a finite γ_{12} that is 'not' at its minimum (represented by the line connecting points A, B, and C in Figure 4.3). Hence, while the association between the vanishing of g_{12} and the minimum value of γ_{12} holds approximately true under the condition of long distances, it is not a comprehensive criterion in all situations, particularly when different polarizations and short distances are involved.

Fig. 4.2(b) illustrates a equilateral triangle configuration where the interparticle distance is set to the magic spacing $s_{\mu\nu} = s_m$. This configuration serves as an example for extending the analysis to the case of two atoms. In this arrangement, all the mutual en-

doi:10.6342/NTU202300902

ergy shifts and decay rates exhibit equivalence to the two-atom case arranged in a linear configuration. The coupling strength $g_{\mu\nu}$ vanishes simultaneously in these configurations, resulting in optimal cooling performance. We note that a finite region exhibiting enhanced cooling performance can also be observed for s_{12} around s_m, where the absolute value of g_{12} emerges and compromises the cooling performance.

4.2 Dipole polarization and magic spacings

We further investigate the impact of varying the polarization angles θ on the emergence of magic spacings in two-atom configuration. The polarization angle impacts the short-range characteristics of collective energy shifts, leading to an increased number of crossing points at $g_{12} = 0$ as θ is varied. In Fig. 4.3(a), we identify these magic spacings by locating the crossing points where $g_{12}(s_{12}, \theta) = 0$, specifically focusing on s_{12} values that are less than or equal to λ. As θ approaches zero, the polarization becomes parallel to the line axis connecting the two atoms and there emerges more magic spacings, offering potential enhancements in cooling behavior. To analyze the changes, we select six representative points labeled as A to F, tracking their corresponding variations in the collective decay rates, γ_{12}, shown in Fig. 4.3(b), and cooling performance displayed in Fig. 4.3(c). In the case of $s_{12} > \lambda$, the decay rate γ_{12} in Equation (2.17) weakens proportionally as $1/\xi$ at longer distances. This transition moves the system towards a noninteracting regime with reduced significance of RDDIs. Point F, located approximately at $\theta \approx \pi/2$, corresponding to the case shown in Figure 4.2, where the cooling enhancement is small, resulting in a 5% reduction compared to the single atom limit, indicated by $\langle n_1 \rangle_{multi}/\langle n_1 \rangle_{single} \approx 0.95$.

The changes in γ_{12} and cooling behaviors corresponding to the magic spacings shown

doi:10.6342/NTU202300902

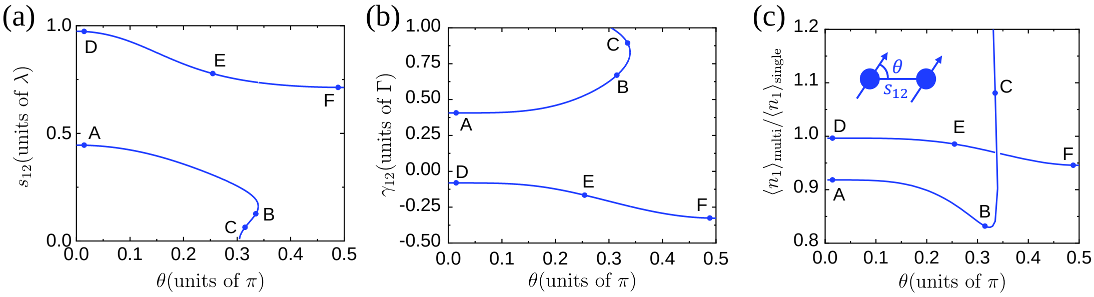

Figure 4.3: Identification of magic spacings, along with the corresponding collective decay rate, and cooling enhancement in a two-atom case. (a) The plot shows solid lines denoting the (s_{12}, θ) values for which the frequency shifts $g_{12}(s_{12}, \theta)$ vanish, where θ is defined as the angle between the interatomic distance and the dipole moment direction. The identified magic spacings, labeled as A to F, showcase varied cooling behaviors under different parameters. (b) and (c) respectively show the corresponding collective decay rates γ_{12} and cooling enhancement. An inset plot in (c) clearly defines θ. Several magic spacings emerge at $g_{12} = 0$ while varying θ. The remaining system parameters remain the same as depicted in Figure 4.2. This figure has been adapted from [1]

in Figure 4.3(a) can be traced in Figures 4.3(b) and 4.3(c). The positive and negative values of γ_{12} align with the set of magic spacings, specifically when interatomic distance s_{12} equals to the magic spacings s_m determined by the zero points of g_{12}. When θ is approximately less than 0.35π, multiple oscillations of g_{12} occur when atomic distance is less than λ. In this range, an optimal cooling enhancement appears near point B, exhibiting about 17% photon ratio reduction from the single atom case.

Along the trajectory from points A to C, significant values of $|\gamma_{12}|$ are found, approximately exceeding 0.5Γ when compared to the values along the D-E-F path. This highlights the emergence of an optimal cooling condition with a finite $|\gamma_{12}|$ satisfying the inequality $0.5\Gamma \lesssim |\gamma_{12}| \lesssim 0.8\Gamma$, representing a regime of moderate interaction where $\gamma_{12} \approx 0.4\Gamma$ at point A, and a heating regime where γ_{12} approaches Γ (point C). In the moderately interacting regime, RDDIs contribute to the cooling mechanism by removing excess heat with the assistance of a finite $\Gamma - |\gamma_{12}|$ in the atom-waveguide system's unguided modes. Conversely, near point C, where the magic spacing is very close to 0.05λ, the system enters a strongly interacting regime characterized by Dicke superradiance and high spin-spin correlations, resulting in heating effects instead.

As we examine the sequence of points D-E-F, the system gradually transitions towards the noninteracting regime where $|\gamma_{12}|$ approaches zero. In this regime, the influence of RDDIs disappears, and the cooling performance converges towards the single atom case without significant enhancements. This is evident at point D, where $\langle n_1\rangle_{multi}/\langle n_1\rangle_{single}$ is approximately equal to 1. When comparing points A and F, we observe that $|\gamma_{12}|$ is slightly higher at A than at F, resulting in a slightly more pronounced cooling enhancement at A, as illustrated in Figure 4.3(c).

4.3 Effect of laser detuning and collective frequency shift

We now relax the requirement of exact sideband cooling, where $\Delta = -\nu$, and explore the influence of laser detuning on the cooling enhancement of individual systems. As demonstrated in Figure 4.4(a), when the atomic spacing s_{12} deviates from s_m, a non-zero collective frequency shift $\Omega_s = g_{12}$ emerges. This shift reduces the optimal cooling performance. However, it can be compensated for by adjusting the detuning of the driving field. Consequently, it is expected that employing a laser field with a detuning away from the conventional sideband cooling condition could introduce new parameter ranges for achieving cooling objectives.

In Fig. 4.4(b), we have performed numerical calculations to examine the cooling performance as a function of both the laser detuning and the interparticle distance in a two-atom system. We observe that the magic spacing identified in Fig. 4.2 emerges when the exact sideband cooling condition of $\Delta = -\nu$ is imposed. However, when this condition is relaxed, we find another magic spacing at $s_{12} \approx 0.25\lambda$ when $\Delta + \nu \approx -0.3\Gamma$, which

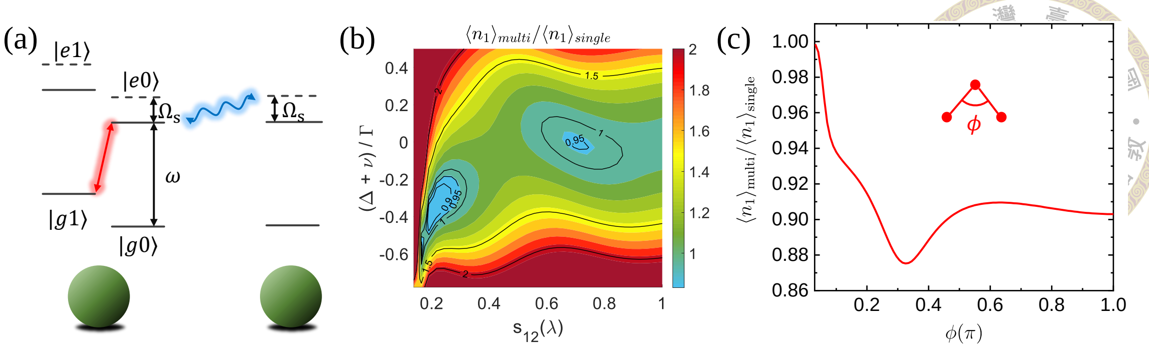

Figure 4.4: The demonstration showing how the efficiency of cooling is influenced by the detuning of the laser and the collective frequency shift. (a) A schematic diagram illustrates how the presence of non-zero collective frequency shift Ω_s affects the spin-exchange interactions (blue arrow), resulting in reduced cooling performance once the laser is set to the regular red-sideband condition (red arrow). (b) Cooling efficiency is depicted as a function of laser detuning and particle spacings for a two-atom system. (c) We consider an isosceles triangle configuration with equilateral interatomic distances being magic spacing $s_m \approx 0.71\lambda$, where the optimal enhancement is achieved at $\phi = \pi/3$ for the target atom at the apex, with negligible collective frequency shifts for all atoms. Other three-atom configurations at different angles ϕ, such as a line shape at $\phi = \pi$, exhibit a reduced exchange process due to non-vanishing Ω_s, resulting in reduced but still better cooling performance compared to the single-atom case. The remaining parameters are consistent with those described in Fig. 4.2. This figure has been adapted from [1]

corresponds to $g_{12} \approx 0.3\Gamma$, as shown in Fig. 4.2(a). This suggests that the frequency shift induced by the DDI can be compensated by the laser detuning, and the cooling performance at this second magic spacing surpasses that of the previously identified one in Fig. 4.2(b).

Two regions of superior cooling performance are indicated in the Fig 4.4(b), but it should be noted that both g_{12} and γ_{12} need to be taken into account simultaneously. Therefore, it is not guaranteed that an enhanced cooling effect will occur when $\Delta + g_{12} \approx -\nu$ without a significant $|\gamma_{12}|$. For example, the region where $s_{12} \to \lambda$ approximately satisfies this condition but does not show superior cooling performance. When considering interparticle distances $s_{12} \leq 0.2\lambda$, a narrow and diminishing region of enhanced cooling emerges due to the abrupt rise in g_{12}. To counteract this effect before the heating mechanism becomes dominant as γ_{12} approaches Γ, a larger red detuning of the laser field is required. Analogous heating effects can also be observed at point C in Figures 4.3(b) and 4.3(c).

We investigates an isosceles triangle configuration in Figure 4.4(c) , where the target atom is positioned at the top vertex of the triangle, and the side lengths are equal to s_m to ensure zero collective frequency shifts. By varying the angle ϕ, we introduce a finite and variable collective energy shift between the spectator atoms, consequently affecting the cooling performance of the target. The most efficient cooling is achieved when ϕ equals $\pi/3$. This, combined with the findings from Fig. 2(b), suggests that optimal cooling performance is favored by an equilateral triangle configuration in the $\phi - s_{12}$ parameter space. This highlights the significance of frequency shifts on the spectator atoms depicted in Fig. 4.4(c), indicating that these frequency shifts have a detrimental impact on the cooling efficiency. An optimal value of $\langle n_1 \rangle_{multi} / \langle n_1 \rangle_{single} \approx 0.87$ can be attained, demonstrating enhanced cooling across a wide range of ϕ values, except when ϕ approaches 0. In the latter case, the frequency shift between the spectator atoms diverges, leading to a single atom cooling performance. This phenomenon implies the suppression of collective spin-exchange interactions due to non-resonant light-atom couplings, rendering the cooling mechanism ineffective.

4.4 Multiatom configurations

In this final section, we extend our investigation to multiatom configurations based on the insights gained from our previous analyses. We have established that achieving optimal enhanced cooling performance requires avoiding collective frequency shifts on the target atom in the context of sideband cooling. With this consideration in mind, we

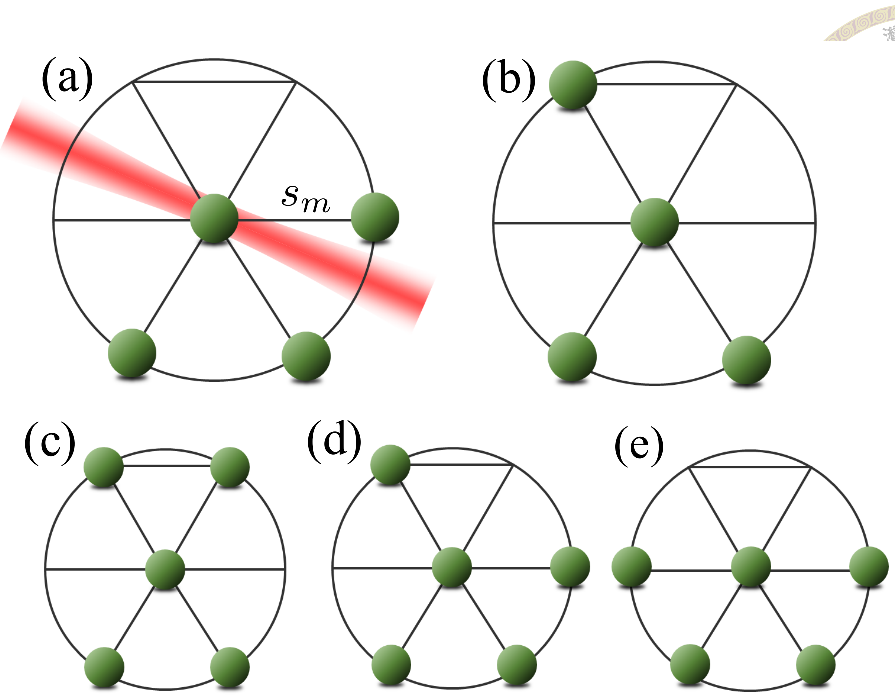

Figure 4.5: Various 4- and 5-atom configurations, positioned at the center and vertices of a hexagon, are examined to investigate the effect on cooling enhancement. The target atom is located at the center of the hexagon, with the and the lattice spacing of this hexagon is set to be magic spacing s_m. The ratio of the normalized phonon occupation of the target atom in the multi-atom configuration, $\langle n_1\rangle_{multi}$, to the single-atom case, $\langle n_1\rangle_{single}$,which indicates the cooling performance, is measured. The obtained ratios, $0.863, 0.864, 0.842, 0.849$ and 0.890, for configurations (a-e) respectively, indicate a moderate enhancement in cooling compared to the cases of $N = 2$ and 3 shown in Figs. 4.2(b) and 4.4(c). This figure has been adapted from [1]

explore a hexagonal structure where the target atom occupies the central position, and the remaining spectator atoms are positioned at the vertices of the hexagon. We examine configurations involving up to five atoms in total. By setting the side lengths of the hexagon to be equal to the magic spacing, we ensure that the target atom experiences zero frequency shifts resulting from RDDIs with the other atoms. This allows us to investigate the impact of the multiatom structure on the cooling performance of the target atom.

In Fig. 4.5, we observe two possible alignments of the laser beam: it can either be precisely directed onto the target atom within the plane of atoms, or it can have a slightly off-plane angle, fulfilling the asymmetric driving condition. As the number of atoms increases, a moderate enhancement in cooling performance is observed, with $\langle n_1\rangle_{multi}/\langle n_1\rangle_{single}$

approximately equal to 0.8 for $N = 5$, compared to 0.95 for $N = 2$ and 0.87 for $N = 3$. However, we also note that the cooling performance reaches a saturation point, and even exhibits slightly diminished enhancement in Fig. 4.5(e). This can be attributed to the presence of finite frequency shifts between the spectator atoms, which can not be completely eliminated when additional atoms are added around the target atom, despite the elimination of shifts from nearest neighbors. This indicates a decrease in the impact of multiatom enhancement on cooling. Additionally, it is crucial to recognize that a three-dimensional atomic arrangement does not resolve this matter since it introduces new projection angles between light polarizations and interparticle axes, resulting in non-zero energy shifts on the target atom.

Chapter5

Conclusion

The dark-state sideband cooling method investigated in this study is applicable to both two-level and three-level atomic systems. The laser parameters can be tailored to achieve resolved sideband cooling, making it a versatile technique. By utilizing resonant dipole-dipole interactions in precisely arranged atomic arrays, our findings can lead to subrecoil cooling of trapped atoms with exceptional performance [4, 71]. The use of long-range spin-exchange interactions, facilitated by an asymmetric driving condition, enables the removal of excess heat and results in improved cooling behavior. The precise positioning of atoms can be achieved using versatile and adaptable optical tweezer arrays [51], which have proven effective for manipulating neutral atoms, molecules, and ions. The laser cooling technique presented in this work offers several advantages, including the rapid preparation of the motional ground state without relying on atom-atom collisions as in evaporative cooling [72, 73]. Our study shows the potential of RDDIs and their collective behavior in generating significant spin-phonon correlations among atoms. Moreover, it unveils new parameter regimes that facilitate distinct cooling mechanisms.

To summarize, our investigation focuses on the application of resonant dipole-dipole

doi:10.6342/NTU202300902

interactions in the dark-state sideband cooling of trapped atoms in free space. Our results reveal that this approach surpasses traditional resolved sideband cooling techniques in single atoms, leading to enhanced cooling performance and driving the atom towards its motional ground state through spontaneous emissions. We further demonstrate that optimal cooling behavior is achieved by placing the atoms at specific magic interparticle distances, where the collective frequency shifts on the target atom become negligible. Additionally, we show that the cooling performance can be further improved in various multiatom configurations by adjusting laser detuning and light polarization angles. This study sheds light on the subrecoil cooling of atoms using collective DDIs in free space, offering promising prospects for overcoming cooling limitations in scalable quantum computation and quantum simulations.

doi:10.6342/NTU202300902

References

[1] Chung-Hsien Wang, Yi-Cheng Wang, Chi-Chih Chen, Chun-Che Wang, and H. H. Jen. Enhanced dark-state sideband cooling in trapped atoms via photon-mediated dipole-dipole interactions. Phys. Rev. A, 107:023117, Feb 2023.

[2] Vladan Vuletić, Cheng Chin, Andrew J. Kerman, and Steven Chu. Degenerate raman sideband cooling of trapped cesium atoms at very high atomic densities. Phys. Rev. Lett., 81:5768–5771, Dec 1998.

[3] Immanuel Bloch. Ultracold quantum gases in optical lattices. Nature Physics, 1(1):23–30, Oct 2005.

[4] Daniel Barredo, Sylvain de Léséleuc, Vincent Lienhard, Thierry Lahaye, and Antoine Browaeys. An atom-by-atom assembler of defect-free arbitrary two-dimensional atomic arrays. Science, 354(6315):1021–1023, 2016.

[5] Ryuta Yamamoto, Hideki Ozawa, David C. Nak, Ippei Nakamura, and Takeshi Fukuhara. Single-site-resolved imaging of ultracold atoms in a triangular optical lattice. New Journal of Physics, 22(12):123028, dec 2020.

[6] M. D. Lukin and P. R. Hemmer. Quantum entanglement via optical control of atom-atom interactions. Phys. Rev. Lett., 84:2818–2821, Mar 2000.

doi:10.6342/NTU202300902

[7] Avikar Periwal, Eric S. Cooper, Philipp Kunkel, Julian F. Wienand, Emily J. Davis, and Monika Schleier-Smith. Programmable interactions and emergent geometry in an array of atom clouds. Nature, 600(7890):630–635, Dec 2021.

[8] D. Leibfried, R. Blatt, C. Monroe, and D. Wineland. Quantum dynamics of single trapped ions. Rev. Mod. Phys., 75:281–324, Mar 2003.

[9] Immanuel Bloch, Jean Dalibard, and Sylvain Nascimbène. Quantum simulations with ultracold quantum gases. Nature Physics, 8(4):267–276, Apr 2012.

[10] Iulia Buluta and Franco Nori. Quantum simulators. Science, 326(5949):108–111, 2009.

[11] B. P. Lanyon, C. Hempel, D. Nigg, M. Müller, R. Gerritsma, F. Zähringer, P. Schindler, J. T. Barreiro, M. Rambach, G. Kirchmair, M. Hennrich, P. Zoller, R. Blatt, and C. F. Roos. Universal digital quantum simulation with trapped ions. Science, 334(6052):57–61, 2011.

[12] C. Monroe, W. C. Campbell, L.-M. Duan, Z.-X. Gong, A. V. Gorshkov, P. W. Hess, R. Islam, K. Kim, N. M. Linke, G. Pagano, P. Richerme, C. Senko, and N. Y. Yao. Programmable quantum simulations of spin systems with trapped ions. Rev. Mod. Phys., 93:025001, Apr 2021.

[13] Hannes Bernien, Sylvain Schwartz, Alexander Keesling, Harry Levine, Ahmed Omran, Hannes Pichler, Soonwon Choi, Alexander S. Zibrov, Manuel Endres, Markus Greiner, Vladan Vuletić, and Mikhail D. Lukin. Probing many-body dynamics on a 51-atom quantum simulator. Nature, 551(7682):579–584, Nov 2017.

[14] Sepehr Ebadi, Tout T. Wang, Harry Levine, Alexander Keesling, Giulia Semeghini, Ahmed Omran, Dolev Bluvstein, Rhine Samajdar, Hannes Pichler, Wen Wei Ho,

doi:10.6342/NTU202300902

Soonwon Choi, Subir Sachdev, Markus Greiner, Vladan Vuletić, and Mikhail D. Lukin. Quantum phases of matter on a 256-atom programmable quantum simulator. Nature, 595(7866):227–232, Jul 2021.

[15] J. I. Cirac and P. Zoller. Quantum computations with cold trapped ions. Phys. Rev. Lett., 74:4091–4094, May 1995.

[16] D. Kielpinski, C. Monroe, and D. J. Wineland. Architecture for a large-scale ion-trap quantum computer. Nature, 417(6890):709–711, Jun 2002.

[17] J. M. Pino, J. M. Dreiling, C. Figgatt, J. P. Gaebler, S. A. Moses, M. S. Allman, C. H. Baldwin, M. Foss-Feig, D. Hayes, K. Mayer, C. Ryan-Anderson, and B. Neyenhuis. Demonstration of the trapped-ion quantum ccd computer architecture. Nature, 592(7853):209–213, Apr 2021.

[18] Dolev Bluvstein, Harry Levine, Giulia Semeghini, Tout T. Wang, Sepehr Ebadi, Marcin Kalinowski, Alexander Keesling, Nishad Maskara, Hannes Pichler, Markus Greiner, Vladan Vuletić, and Mikhail D. Lukin. A quantum processor based on coherent transport of entangled atom arrays. Nature, 604(7906):451–456, Apr 2022.

[19] T. M. Graham, Y. Song, J. Scott, C. Poole, L. Phuttitarn, K. Jooya, P. Eichler, X. Jiang, A. Marra, B. Grinkemeyer, M. Kwon, M. Ebert, J. Cherek, M. T. Lichtman, M. Gillette, J. Gilbert, D. Bowman, T. Ballance, C. Campbell, E. D. Dahl, O. Crawford, N. S. Blunt, B. Rogers, T. Noel, and M. Saffman. Multi-qubit entanglement and algorithms on a neutral-atom quantum computer. Nature, 604(7906):457–462, Apr 2022.

[20] J. I. Cirac and P. Zoller. A scalable quantum computer with ions in an array of microtraps. Nature, 404(6778):579–581, Apr 2000.

[21] F. Diedrich, J. C. Bergquist, Wayne M. Itano, and D. J. Wineland. Laser cooling to the zero-point energy of motion. Phys. Rev. Lett., 62:403–406, Jan 1989.

[22] C. Monroe, D. M. Meekhof, B. E. King, S. R. Jefferts, W. M. Itano, D. J. Wineland, and P. Gould. Resolved-sideband raman cooling of a bound atom to the 3d zero-point energy. Phys. Rev. Lett., 75:4011–4014, Nov 1995.

[23] J. I. Cirac, R. Blatt, P. Zoller, and W. D. Phillips. Laser cooling of trapped ions in a standing wave. Phys. Rev. A, 46:2668–2681, Sep 1992.

[24] Ch. Roos, Th. Zeiger, H. Rohde, H. C. Nägerl, J. Eschner, D. Leibfried, F. Schmidt-Kaler, and R. Blatt. Quantum state engineering on an optical transition and decoherence in a paul trap. Phys. Rev. Lett., 83:4713–4716, Dec 1999.

[25] A. M. Kaufman, B. J. Lester, and C. A. Regal. Cooling a single atom in an optical tweezer to its quantum ground state. Phys. Rev. X, 2:041014, Nov 2012.

[26] Giovanna Morigi, Jürgen Eschner, and Christoph H. Keitel. Ground state laser cooling using electromagnetically induced transparency. Phys. Rev. Lett., 85:4458–4461, Nov 2000.

[27] C. F. Roos, D. Leibfried, A. Mundt, F. Schmidt-Kaler, J. Eschner, and R. Blatt. Experimental demonstration of ground state laser cooling with electromagnetically induced transparency. Phys. Rev. Lett., 85:5547–5550, Dec 2000.

[28] J. Cerrillo, A. Retzker, and M. B. Plenio. Fast and robust laser cooling of trapped systems. Phys. Rev. Lett., 104:043003, Jan 2010.

[29] Tobias Kampschulte, Wolfgang Alt, Sebastian Manz, Miguel Martinez-Dorantes, René Reimann, Seokchan Yoon, Dieter Meschede, Marc Bienert, and Giovanna Mo-

doi:10.6342/NTU202300902

rigi. Electromagnetically-induced-transparency control of single-atom motion in an optical cavity. Phys. Rev. A, 89:033404, Mar 2014.

[30] Elena Jordan, Kevin A. Gilmore, Athreya Shankar, Arghavan Safavi-Naini, Justin G. Bohnet, Murray J. Holland, and John J. Bollinger. Near ground-state cooling of two-dimensional trapped-ion crystals with more than 100 ions. Phys. Rev. Lett., 122:053603, Feb 2019.

[31] Mu Qiao, Ye Wang, Zhengyang Cai, Botao Du, Pengfei Wang, Chunyang Luan, Wentao Chen, Heung-Ryoul Noh, and Kihwan Kim. Double-electromagnetically-induced-transparency ground-state cooling of stationary two-dimensional ion crystals. Phys. Rev. Lett., 126:023604, Jan 2021.

[32] Athreya Shankar, Elena Jordan, Kevin A. Gilmore, Arghavan Safavi-Naini, John J. Bollinger, and Murray J. Holland. Modeling near ground-state cooling of two-dimensional ion crystals in a penning trap using electromagnetically induced transparency. Phys. Rev. A, 99:023409, Feb 2019.

[33] R. H. Lehmberg. Radiation from an n-atom system. i. general formalism. Phys. Rev. A, 2:883–888, Sep 1970.

[34] E. V. Goldstein, P. Pax, and P. Meystre. Dipole-dipole interaction in three-dimensional optical lattices. Phys. Rev. A, 53:2604–2615, Apr 1996.

[35] Z. Meir, O. Schwartz, E. Shahmoon, D. Oron, and R. Ozeri. Cooperative lamb shift in a mesoscopic atomic array. Phys. Rev. Lett., 113:193002, Nov 2014.

[36] Jun Rui, David Wei, Antonio Rubio-Abadal, Simon Hollerith, Johannes Zeiher, Dan M. Stamper-Kurn, Christian Gross, and Immanuel Bloch. A subradiant opti-

doi:10.6342/NTU202300902

cal mirror formed by a single structured atomic layer. Nature, 583(7816):369–374, Jul 2020.

[37] Chi-Chih Chen, Yi-Cheng Wang, Chun-Che Wang, and H H Jen. Chiral-coupling-assisted refrigeration in trapped ions. Journal of Physics B: Atomic, Molecular and Optical Physics, 56(10):105502, apr 2023.

[38] Minghui Xu, Simon B. Jäger, S. Schütz, J. Cooper, Giovanna Morigi, and M. J. Holland. Supercooling of atoms in an optical resonator. Phys. Rev. Lett., 116:153002, Apr 2016.

[39] Chun-Che Wang, Yi-Cheng Wang, Chung-Hsien Wang, Chi-Chih Chen, and H H Jen. Superior dark-state cooling via nonreciprocal couplings in trapped atoms. New Journal of Physics, 24(11):113020, nov 2022.

[40] S. D. Jenkins, J. Ruostekoski, J. Javanainen, S. Jennewein, R. Bourgain, J. Pellegrino, Y. R. P. Sortais, and A. Browaeys. Collective resonance fluorescence in small and dense atom clouds: Comparison between theory and experiment. Phys. Rev. A, 94:023842, Aug 2016.

[41] R. T. Sutherland and F. Robicheaux. Collective dipole-dipole interactions in an atomic array. Phys. Rev. A, 94:013847, Jul 2016.

[42] Anatoly A. Svidzinsky, Jun-Tao Chang, and Marlan O. Scully. Cooperative spontaneous emission of n atoms: Many-body eigenstates, the effect of virtual lamb shift processes, and analogy with radiation of n classical oscillators. Phys. Rev. A, 81:053821, May 2010.

[43] Marlan O. Scully. Collective lamb shift in single photon dicke superradiance. Phys. Rev. Lett., 102:143601, Apr 2009.

[44] Antoine Glicenstein, Giovanni Ferioli, Nikola Šibalić, Ludovic Brossard, Igor Ferrier-Barbut, and Antoine Browaeys. Collective shift in resonant light scattering by a one-dimensional atomic chain. Phys. Rev. Lett., 124:253602, Jun 2020.

[45] Mira Maiwöger, Matthias Sonnleitner, Tiantian Zhang, Igor Mazets, Marion Mallweger, Dennis Rätzel, Filippo Borselli, Sebastian Erne, Jörg Schmiedmayer, and Philipp Haslinger. Observation of light-induced dipole-dipole forces in ultracold atomic gases. Phys. Rev. X, 12:031018, Jul 2022.

[46] R. H. Dicke. Coherence in spontaneous radiation processes. Phys. Rev., 93:99–110, Jan 1954.

[47] Eric Sierra, Stuart J. Masson, and Ana Asenjo-Garcia. Dicke superradiance in ordered lattices: Dimensionality matters. Phys. Rev. Res., 4:023207, Jun 2022.

[48] Michelle O. Araújo, Ivor Krešić, Robin Kaiser, and William Guerin. Superradiance in a large and dilute cloud of cold atoms in the linear-optics regime. Phys. Rev. Lett., 117:073002, Aug 2016.

[49] Jinuk Kim, Seung-hoon Oh, Daeho Yang, Junki Kim, Moonjoo Lee, and Kyungwon An. A photonic quantum engine driven by superradiance. Nature Photonics, Jul 2022.

[50] Yi-Cheng Wang, Jhih-Shih You, and H. H. Jen. A non-hermitian optical atomic mirror. Nature Communications, 13(1):4598, Aug 2022.

[51] Loïc Anderegg, Lawrence W. Cheuk, Yicheng Bao, Sean Burchesky, Wolfgang Ketterle, Kang-Kuen Ni, and John M. Doyle. An optical tweezer array of ultracold molecules. Science, 365(6458):1156–1158, 2019.

[52] Yu-Ching Shen and Guin-Dar Lin. Scalable quantum computing stabilised by optical tweezers on an ion crystal. New Journal of Physics, 22(5):053032, may 2020.

[53] Immanuel Bloch, Jean Dalibard, and Wilhelm Zwerger. Many-body physics with ultracold gases. Rev. Mod. Phys., 80:885–964, Jul 2008.

[54] Klemens Hammerer, Anders S. Sørensen, and Eugene S. Polzik. Quantum interface between light and atomic ensembles. Rev. Mod. Phys., 82:1041–1093, Apr 2010.

[55] S. Rebić, D. Vitali, C. Ottaviani, P. Tombesi, M. Artoni, F. Cataliotti, and R. Corbalán. Polarization phase gate with a tripod atomic system. Phys. Rev. A, 70:032317, Sep 2004.

[56] E. Peter, P. Senellart, D. Martrou, A. Lemaître, J. Hours, J. M. Gérard, and J. Bloch. Exciton-photon strong-coupling regime for a single quantum dot embedded in a microcavity. Phys. Rev. Lett., 95:067401, Aug 2005.

[57] Shuo Zhang, Jian-Qi Zhang, Wei Wu, Wan-Su Bao, and Chu Guo. Fast cooling of trapped ion in strong sideband coupling regime. New Journal of Physics, 23(2):023018, feb 2021.

[58] L. Feng, W. L. Tan, A. De, A. Menon, A. Chu, G. Pagano, and C. Monroe. Efficient ground-state cooling of large trapped-ion chains with an electromagnetically-induced-transparency tripod scheme. Phys. Rev. Lett., 125:053001, Jul 2020.

[59] D. J. Wineland and Wayne M. Itano. Laser cooling of atoms. Phys. Rev. A, 20:1521–1540, Oct 1979.

[60] Stig Stenholm. The semiclassical theory of laser cooling. Rev. Mod. Phys., 58:699–739, Jul 1986.

doi:10.6342/NTU202300902

[61] A. Aspect, E. Arimondo, R. Kaiser, N. Vansteenkiste, and C. Cohen-Tannoudji. Laser cooling below the one-photon recoil energy by velocity-selective coherent population trapping. Phys. Rev. Lett., 61:826–829, Aug 1988.

[62] Yong Lu, Jian-Qi Zhang, Jin-Ming Cui, Dong-Yang Cao, Shuo Zhang, Yun-Feng Huang, Chuan-Feng Li, and Guang-Can Guo. Dark-state cooling of a trapped ion using microwave coupling. Phys. Rev. A, 92:023420, Aug 2015.

[63] D. S. Naik, H. Eneriz-Imaz, M. Carey, T. Freegarde, F. Minardi, B. Battelier, P. Bouyer, and A. Bertoldi. Loading and cooling in an optical trap via hyperfine dark states. Phys. Rev. Res., 2:013212, Feb 2020.

[64] Chang Huang, Shijie Chai, and Shau-Yu Lan. Dark-state sideband cooling in an atomic ensemble. Phys. Rev. A, 103:013305, Jan 2021.

[65] Regina Lechner, Christine Maier, Cornelius Hempel, Petar Jurcevic, Ben P. Lanyon, Thomas Monz, Michael Brownnutt, Rainer Blatt, and Christian F. Roos. Electromagnetically-induced-transparency ground-state cooling of long ion strings. Phys. Rev. A, 93:053401, May 2016.

[66] Nils Scharnhorst, Javier Cerrillo, Johannes Kramer, Ian D. Leroux, Jannes B. Wübbena, Alex Retzker, and Piet O. Schmidt. Experimental and theoretical investigation of a multimode cooling scheme using multiple electromagnetically-induced-transparency resonances. Phys. Rev. A, 98:023424, Aug 2018.

[67] Elmar Haller, James Hudson, Andrew Kelly, Dylan A. Cotta, Bruno Peaudecerf, Graham D. Bruce, and Stefan Kuhr. Single-atom imaging of fermions in a quantum-gas microscope. Nature Physics, 11(9):738–742, Sep 2015.

[68] G. J. A. Edge, R. Anderson, D. Jervis, D. C. McKay, R. Day, S. Trotzky, and J. H. Thywissen. Imaging and addressing of individual fermionic atoms in an optical lattice. Phys. Rev. A, 92:063406, Dec 2015.

[69] R. Mitsch, C. Sayrin, B. Albrecht, P. Schneeweiss, and A. Rauschenbeutel. Quantum state-controlled directional spontaneous emission of photons into a nanophotonic waveguide. Nature Communications, 5(1):5713, Dec 2014.

[70] Peter Lodahl, Sahand Mahmoodian, Søren Stobbe, Arno Rauschenbeutel, Philipp Schneeweiss, Jürgen Volz, Hannes Pichler, and Peter Zoller. Chiral quantum optics. Nature, 541(7638):473–480, Jan 2017.

[71] Manuel Endres, Hannes Bernien, Alexander Keesling, Harry Levine, Eric R. Anschuetz, Alexandre Krajenbrink, Crystal Senko, Vladan Vuletic, Markus Greiner, and Mikhail D. Lukin. Atom-by-atom assembly of defect-free one-dimensional cold atom arrays. Science, 354(6315):1024–1027, 2016.

[72] J. D. Thompson, T. G. Tiecke, A. S. Zibrov, V. Vuletić, and M. D. Lukin. Coherence and raman sideband cooling of a single atom in an optical tweezer. Phys. Rev. Lett., 110:133001, Mar 2013.

[73] Adam M. Kaufman and Kang-Kuen Ni. Quantum science with optical tweezer arrays of ultracold atoms and molecules. Nature Physics, 17(12):1324–1333, Dec 2021.

Appendix A — Derivation of Photon - mediated Dipole-Dipole Interaction

In Section 2.3, we simplified the equation of motion to a reduced form that depends solely on the current atomic operators. The subsequent step involves evaluating the remaining integral. We note that the conjugate part in equation (2.8) is included in solving the integral given by:

$$\int d\Omega(1-(d\hat{\Omega}\cdot\hat{\mathbf{d}})^2)\int_{-\infty}^{\infty} d\omega\omega^3 e^{i\omega d\hat{\Omega}\cdot\mathbf{r}_{\mu\nu}/c}\int_0^{\infty} dt e^{-i(\omega\pm\omega_0)t} \tag{A.1}$$

Utilizing the common spherical surface parameterization in θ and ϕ coordinates, we may perform the angular integration. We may also choose to set $\mathbf{r}_{\mu\nu}=r_{\mu\nu}\hat{z}$ and $\hat{\mathbf{d}}=\cos\theta\hat{z}+\sin\theta\hat{x}$ on the xz plane without loss of generality owing to symmetry. The resulting angular integral may then be expressed in terms of the function $F_{\mu\nu}(x)$, given by:

$$\int d\Omega(1-(d\hat{\Omega}\cdot\hat{\mathbf{d}})^2)e^{i\omega d\hat{\Omega}\cdot\mathbf{r}_{\mu\nu}/c}=4\pi F_{\mu\nu}\left(\frac{\omega r_{\mu\nu}}{c}\right) \tag{A.2}$$

Such that

$$F_{\mu\nu}(x)=(1-\cos^2\theta)\frac{\sin x}{x}+(1-3\cos^2\theta)\left(\frac{\cos x}{x^2}-\frac{\sin x}{x^3}\right) \tag{A.3}$$

doi:10.6342/NTU202300902

where $\cos\theta \equiv \hat{\mathbf{d}} \cdot \hat{\mathbf{r}}_{\mu\nu}$ denotes the angle between the dipole polarization and the atom connection line.

The Kramers-Kronig relations can be used to replace the time integral in the expression as a sum of a Dirac delta function and a Cauchy principal value:

$$\int_0^\infty dt e^{-i(\omega\pm\omega_0)t} = \pi\delta(\omega\pm\omega_0) - i\mathcal{P}\left(\frac{1}{\omega\pm\omega_0}\right) \tag{A.4}$$

where $\mathcal{P}$ denotes the Cauchy principal value. So the final angular integral reads:

$$\int_{-\infty}^\infty d\omega\omega^3 4\pi F_{\mu\nu}\left(\frac{\omega r_{\mu\nu}}{c}\right)\left(\pi\delta(\omega\pm\omega_0) - i\mathcal{P}\left(\frac{1}{\omega\pm\omega_0}\right)\right) \tag{A.5}$$

The Cauchy principal value is evaluated using the Sokhotski-Plemelj theorem, which involves taking the mean-value of the integrals with the pole slightly displaced above and below, resulting some integrals of the form:

$$\begin{aligned}\lim_{\epsilon\to 0}\frac{1}{2}\left[\int_{-\infty}^\infty d\omega \sin\left(\frac{\omega r_{\mu\nu}}{c}\right)\frac{\omega^n}{\omega-\omega_0+i\epsilon} + \int_{-\infty}^\infty d\omega \sin\left(\frac{\omega r_{\mu\nu}}{c}\right)\frac{\omega^n}{\omega-\omega_0-i\epsilon}\right] \\ = \pi\omega_0^n \cos\left(\frac{\omega_0 r_{\mu\nu}}{c}\right),\end{aligned} \tag{A.6}$$

and similarly

$$\begin{aligned}\lim_{\epsilon\to 0}\frac{1}{2}\left[\int_{-\infty}^\infty d\omega \cos\left(\frac{\omega r_{\mu\nu}}{c}\right)\frac{\omega^n}{\omega-\omega_0+i\epsilon} + \int_{-\infty}^\infty d\omega \cos\left(\frac{\omega r_{\mu\nu}}{c}\right)\frac{\omega^n}{\omega-\omega_0-i\epsilon}\right] \\ = -\pi\omega_0^n \sin\left(\frac{\omega_0 r_{\mu\nu}}{c}\right).\end{aligned} \tag{A.7}$$

Thus we see equation (A.5) equals to:

$$4\pi^2\omega_0^3\left(F_{\mu\nu}\left(kr_{\mu\nu}\right) - iG_{\mu\nu}\left(kr_{\mu\nu}\right)\right), \tag{A.8}$$

here $k \equiv \omega_0/c$ and

$$G_{\mu\nu}(x) = -(1-\cos^2\theta)\frac{\cos x}{x} + (1-3\cos^2\theta)\left(\frac{\sin x}{x^2} + \frac{\cos x}{x^3}\right). \tag{A.9}$$

Put back everything in equation (2.8) gives us a whole master equation. Then the rotating-wave approximation is performed by neglecting the fast-rotating terms such as $\sigma_\mu\sigma_\nu$ and $\sigma_\mu\mathbf{E}_0^+$. The resulting master equation is given by:

$$\begin{aligned}&i\omega_0\sum_\mu[\sigma_\mu^\dagger\sigma_\mu, Q] - i\sum_\mu[\sigma_\mu^\dagger, Q]\mathbf{E}_0^+\cdot\mathbf{d} + i[\sigma_\mu, Q]\mathbf{E}_0^-\cdot\mathbf{d}\\ &+\frac{\omega_0^3 d^2}{4\epsilon_0\hbar^3c^3}\sum_{\mu\nu}\left((F_{\mu\nu}-iG_{\mu\nu})[\sigma_\mu^\dagger, Q]\sigma_\nu + (F_{\mu\nu}+iG_{\mu\nu})\sigma_\nu^\dagger[Q,\sigma_\mu]\right)\end{aligned} \tag{A.10}$$

Rearranging the terms. The equation can be written as::

$$\begin{aligned}&\sum_\mu i(\omega_0 - g_{\mu\mu})[\sigma_\mu^\dagger\sigma_\mu, Q] - i\sum_\mu[\sigma_\mu^\dagger, Q]\mathbf{E}_0^+\cdot\mathbf{d} + i[\sigma_\mu, Q]\mathbf{E}_0^-\cdot\mathbf{d}\\ &+i\sum_{\mu\neq\nu}g_{\mu\nu}[\sigma_\mu^\dagger\sigma_\nu, Q] + \sum_{\mu\nu}\frac{\gamma_{\mu\nu}}{2}\left(\sigma_\mu^\dagger Q\sigma_\nu - \frac{1}{2}\{\sigma_\mu^\dagger\sigma_\nu, Q\}\right)\end{aligned} \tag{A.11}$$

where $\gamma_{\mu\nu} = \frac{3\Gamma}{2}F_{\mu\nu}$ and $g_{\mu\nu} = \frac{3\Gamma}{4}G_{\mu\nu}$, while $\Gamma \equiv \frac{\omega_0^3 d^2}{3\epsilon_0\hbar^3c^3}$. The divergent Lamb shift $g_{\mu\mu}$ arises due to the integration over a high frequency region and must be corrected by QED. However, this divergence only contributes to a small shift once renormalized by QED and thus can be absorbed into the definition of the resonance frequency ω_0. For an initial vacuum, the above equation can be expressed in density matrix representation as:

$$\dot\rho = -i[H,\rho] - i\sum_{\mu\neq\nu}g_{\mu\nu}[\sigma_\mu^\dagger\sigma_\nu, \rho] + \sum_{\mu\nu}\frac{\gamma_{\mu\nu}}{2}\left(\sigma_\nu\rho\sigma_\mu^\dagger - \frac{1}{2}\{\sigma_\mu^\dagger\sigma_\nu, \rho\}\right) \tag{A.12}$$